Presynaptic Rac1 controls synaptic strength through the regulation of synaptic vesicle priming

(Abbreviated title): Presynaptic Rac1 regulates synaptic strength

Christian Keine[1,2,3], Mohammed Al-Yaari[1], Tamara Radulovic[1,2,3], Connon I. Thomas[6], Paula Valino Ramos[1], Debbie Guerrero-Given[6], Mrinalini Ranjan[4,5], Holger Taschenberger[4] Naomi Kamasawa[6], and Samuel M. Young, Jr.[1,7^].

[1]Department of Anatomy and Cell Biology, University of Iowa, Iowa City, IA, USA
[2]Department of Human Medicine, Carl-von-Ossietzky University Oldenburg, Oldenburg, Germany
[3]Research Center Neurosensory Science, Oldenburg, Germany
[4]Department of Molecular Neurobiology, Max Planck Institute for Multidisciplinary Sciences, Göttingen, Germany
[5]Göttingen Graduate School for Neurosciences, Biophysics, and Molecular Biosciences, Göttingen, Germany
[6]Electron Microscopy Core Facility, Max Planck Florida Institute, Jupiter, FL, USA
[7]Department of Otolaryngology, Iowa Neuroscience Institute, University of Iowa, Iowa City, IA, USA.

^Correspondence
Samuel M. Young, Jr. PhD
Department of Anatomy and Cell Biology
University of Iowa
PBDB 5322
169 Newton Road
Iowa City, IA 52242
Email: samuel-m-young@uiowa.edu

ORCIDs:

Christian Keine:	0000-0002-8953-2593
Mohammed Al-Yaari	0000-0003-3196-266X
Tamara Radulovic:	0000-0002-2825-9773
Connon I. Thomas:	0000-0003-0995-9667
Mrinalini Ranjan:	0000-0003-4310-3811
Holger Taschenberger:	0000-0003-3186-3231
Naomi Kamasawa:	0000-0002-8926-5309
Samuel M. Young, Jr.:	0000-0002-7589-7612

Abstract

Synapses contain a limited number of synaptic vesicles (SVs) that are released in response to action potentials (APs). Therefore, sustaining synaptic transmission over a wide range of AP firing rates and timescales depends on SV release and replenishment. Although actin dynamics impact synaptic transmission, how presynaptic regulators of actin signaling cascades control SV release and replenishment remains unresolved. Rac1, a Rho GTPase, regulates actin signaling cascades that control synaptogenesis, neuronal development, and postsynaptic function. However, the presynaptic role of Rac1 in regulating synaptic transmission is unclear. To unravel Rac1's roles in controlling transmitter release, we performed selective presynaptic ablation of Rac1 at the mature mouse calyx of Held synapse. Loss of Rac1 increased synaptic strength, accelerated EPSC recovery after conditioning stimulus trains, and augmented spontaneous SV release with no change in presynaptic morphology or AZ ultrastructure. Analyses with constrained short-term plasticity models revealed faster SV priming kinetics and, depending on model assumptions, elevated SV release probability or higher abundance of tightly docked fusion-competent SVs in Rac1-deficient synapses. We conclude that presynaptic Rac1 is a key regulator of synaptic transmission and plasticity mainly by regulating the dynamics of SV priming and potentially SV release probability.

64 **Introduction**

65 Information encoding in the nervous system requires synaptic transmission to drive and sustain
66 action potentials (APs) over rapidly changing and highly variable AP firing rates (Reinagel and
67 Laughlin, 2001; Theunissen and Elie, 2014; Brette, 2015; Azarfar et al., 2018). However, the
68 number of synaptic vesicles (SVs) available for fusion in response to an AP, the readily
69 releasable pool (RRP), is limited (Alabi and Tsien, 2012). Therefore, tight regulation of SV
70 release and RRP replenishment is required for synaptic reliability and temporally precise
71 information encoding (Neher, 2010; Hallermann and Silver, 2013). Priming is the process that
72 generates fusion-competent SVs. It is a critical step in the SV cycle that primarily regulates RRP
73 size and SV pool replenishment. Priming also controls SV release probability (P_r) by determining
74 SV fusogenicity ('molecular priming') and regulating the spatial coupling between docked SV and
75 presynaptic Ca^{2+} entry ('positional priming') (Klug et al., 2012; Schneggenburger and
76 Rosenmund, 2015; Neher and Brose, 2018). In some synapses, the SV priming kinetics are
77 highly dependent on presynaptic cytosolic Ca^{2+} levels, which are activity-dependent. Importantly,
78 human mutations in molecules that regulate priming are associated with neurological disorders
79 (Waites et al., 2011; Wondolowski and Dickman, 2013; Torres et al., 2017; Bonnycastle et al.,
80 2021). Therefore, elucidating the molecular mechanisms that regulate SV priming is critical to
81 understanding the diversity of neuronal information encoding in health and disease.

82 Actin is a central component of both the presynaptic and postsynaptic compartments,
83 with diverse roles in regulating synaptic function and neuronal circuit development. Manipulation
84 of actin dynamics or interference with presynaptic AZ proteins implicated in regulating actin
85 dynamics affects transmitter release and SV replenishment, as well as P_r (Morales et al., 2000;
86 Sakaba and Neher, 2003; Cingolani and Goda, 2008; Sun and Bamji, 2011; Waites et al., 2011;
87 Lee et al., 2012; Lee et al., 2013; Montesinos et al., 2015; Rust and Maritzen, 2015). However,
88 due to disparate results, the role of presynaptic actin signaling cascades in regulating transmitter
89 release and SV pool replenishment is controversial. Finally, in contrast to the postsynaptic

90 compartment, our understanding of how presynaptic regulators of actin signaling cascades
91 control synaptic transmission and short-term plasticity (STP) are in the early stages.

92 Rac1, a Rho GTPase, is a critical regulator of actin signaling cascades (Bosco et al.,
93 2009; Yasuda, 2017), and human mutations in Rac1 are associated with neurological disorders
94 (Bai et al., 2015; Reijnders et al., 2017; Zamboni et al., 2018). Rac1 is involved in multiple
95 processes which control synaptogenesis, axon guidance, neuronal development, and
96 postsynaptic function to regulate neuronal circuit function (Bai et al., 2015). Although Rac1 is
97 expressed in both the pre- and postsynaptic compartment (Threadgill et al., 1997; Doussau et
98 al., 2000; Kumanogoh et al., 2001; O'Neil et al., 2021), its presynaptic role in regulating synaptic
99 transmission is not well understood. Recent work using cultured hippocampal neurons proposed
100 that presynaptic Rac1 is a negative regulator of SV pool replenishment (O'Neil et al., 2021),
101 though at which steps in the SV cycle it exerts its regulatory role is unknown. Finally, how Rac1
102 regulates the temporal dynamics of transmitter release and pool replenishment in a native
103 neuronal circuit remains elusive.

104 To unravel the roles of presynaptic Rac1 in regulating transmitter release, we utilized the
105 calyx of Held, a glutamatergic axosomatic presynaptic terminal in the auditory brainstem, which
106 is the sole input to drive AP firing in the principal cells of the medial nucleus of the trapezoid
107 body (MNTB) (Borst and Soria van Hoeve, 2012; Joris and Trussell, 2018). In the calyx of Held,
108 RRP dynamics are tightly regulated to support a nearly failsafe synaptic transmission with high
109 temporal precision, but the molecular machinery of transmitter release and SV pool
110 replenishment and their regulation are similar to conventional presynaptic terminals in the central
111 nervous system (Iwasaki and Takahashi, 1998; Iwasaki et al., 2000; Iwasaki and Takahashi,
112 2001; Satzler et al., 2002; Taschenberger et al., 2002; Rollenhagen and Lubke, 2006; Neher and
113 Sakaba, 2008; Alabi and Tsien, 2012; Eggermann et al., 2012; Hallermann and Silver, 2013;
114 Schneggenburger and Rosenmund, 2015). In addition, molecular manipulations specific to only
115 the calyceal terminal can be carried out at different developmental stages (Wimmer et al., 2006;

116 Young and Neher, 2009; Chen et al., 2013; Lubbert et al., 2019). To elucidate the roles of
117 presynaptic Rac1 in regulating transmitter release while avoiding interference with its role in
118 synaptogenesis, axon guidance, and neuronal development, we selectively deleted Rac1 two
119 days after hearing onset in postnatal day (P) 14 mouse calyx of Held synapses. At this time
120 point, the synapse is functionally mature, and neuronal properties of brainstem circuits are
121 considered largely "adult-like". Subsequently, we determined how the loss of Rac1 impacted
122 calyx of Held/ MNTB principal cell transmission at the adult stage (P28 onwards) (Sonntag et al.,
123 2009; Crins et al., 2011; Sonntag et al., 2011). Presynaptic Rac1 deletion did neither affect the
124 calyx of Held morphology nor active zone (AZ) ultrastructure but led to increased synaptic
125 strength, faster SV pool replenishment, and augmented spontaneous SV release. Additionally,
126 we found that loss of Rac1 delayed the EPSC onset and potentiated asynchronous release
127 during high-frequency trains.

128 Analysis of the experimental data with constrained STP models confirmed faster SV
129 priming kinetics in Rac1-deficient synapses. Methods of quantal analysis, which assume a single
130 and homogenous pool of readily releasable SVs (Neher, 2015; Schneggenburger and
131 Rosenmund, 2015), reported an increased P_r and a tendency towards an increased RRP after
132 Rac1 loss. Both experimental findings were corroborated in numerical simulation using a single
133 pool STP model (Weis et al., 1999). In contrast, simulations based on a sequential two-step
134 priming scheme which assumes two distinct states of docked/primed SVs, a loosely-docked
135 (LS), immature priming state which is not fusion competent, and a tightly docked (TS), mature
136 priming state which is fusion competent (Neher and Taschenberger, 2021; Lin et al., 2022),
137 required only changes in SV priming kinetics but no change in P_r or the number of release sites
138 to reproduce experimental data. Simulations based on the sequential two-step SV priming and
139 fusion scheme fully accounted for the increased synaptic strength in *Rac1*$^{-/-}$ synapses by a
140 larger abundance of tightly docked SVs. Therefore, we propose that presynaptic Rac1 is a key
141 molecule that controls synaptic strength and STP primarily by regulating the SV priming

142 dynamics and potentially P_r. Finally, we conclude that presynaptic Rac1 is a critical regulator of

143 synaptic transmission and plasticity.

144 **Results**

145 **Presynaptic deletion of Rac1 after hearing onset does not impact calyx of Held**
146 **morphology or AZ ultrastructure**

147 Presynaptic terminals contain Rac1 (Doussau et al., 2000; O'Neil et al., 2021) which regulates
148 synaptogenesis, axon guidance, and neuronal development (Xu et al., 2019; Zhang et al., 2021).
149 In this study, we aimed to elucidate Rac1's presynaptic function in controlling synaptic
150 transmission and plasticity independent of its role in regulating synapse development and
151 maturation at the calyx of Held synapse. To do so, we injected HdAd co-expressing Cre
152 recombinase and EGFP into the cochlear nucleus (CN) of P14 *Rac1*$^{flox/flox}$ mice when the calyx of
153 Held synapse is considered "adult-like" and commenced synapse analysis at P28 onwards (Fig.
154 1A) (Sonntag et al., 2009; Crins et al., 2011; Sonntag et al., 2011). Since Rac1 controls synapse
155 development and morphology, it was essential to determine whether the loss of Rac1 after
156 hearing onset altered the calyx of Held morphology or AZ ultrastructure. We analyzed calyx
157 morphology from 3D reconstructions of confocal z-stack images acquired from *Rac1*$^{+/+}$ and
158 *Rac1*$^{-/-}$ calyces at P28 and found no difference in calyx surface area or volume (Fig. 1B). To
159 determine if the loss of Rac1 impacted AZ ultrastructure, we performed ultrathin-section TEM
160 and analyzed AZ length, SV distribution, and the number of docked SVs and found no difference
161 between *Rac1*$^{+/+}$ and *Rac1*$^{-/-}$ (Fig. 1C). Therefore, we conclude that after hearing onset, Rac1
162 does not regulate calyx of Held morphology and AZ ultrastructure.

163 **Loss of Rac1 increases synaptic strength and relative synaptic depression.**

164 Perturbations of the presynaptic actin cytoskeleton impact synaptic transmission and plasticity in
165 multiple model systems and synapses (Cole et al., 2000; Sakaba and Neher, 2003; Bleckert et
166 al., 2012; Lee et al., 2012; Rust and Maritzen, 2015; Miki et al., 2016; Gentile et al., 2022; Wu
167 and Chan, 2022). Since Rac1 is an actin cytoskeleton regulator, we examined how the loss of
168 Rac1 impacted AP-evoked synaptic transmission and STP. Afferent fibers of calyx synapses
169 were electrically stimulated with 50 APs at two stimulation frequencies (50 and 500 Hz),

170 representing typical *in-vivo* firing rates at the calyx. AMPAR-mediated ESPCs were recorded in
171 MNTB principal cells innervated by transduced (*Rac1*$^{-/-}$) and non-transduced (*Rac1*$^{+/+}$) calyces
172 in 1.2 mM external Ca^{2+} and at 36-37°C to closely mimic *in-vivo* conditions (Fig. 2A, B). By
173 analyzing the initial response ($EPSC_1$) of the EPSC trains, we found a robust increase in
174 synaptic strength upon genetic Rac1 deletion (*Rac*$^{+/+}$ = 1.3 ± 0.4 nA vs. *Rac1*$^{-/-}$ = 3 ± 1.1 nA,
175 $p<0.001$, n = 15/15, Fig. 2C, D1) with no changes in EPSC waveform. Plotting EPSC amplitudes
176 vs. stimulus number revealed substantial differences in STP between *Rac1*$^{+/+}$ and *Rac1*$^{-/-}$
177 synapses. At 50 Hz stimulation, both *Rac1*$^{+/+}$ and *Rac1*$^{-/-}$ showed short-term depression, which
178 was more pronounced in *Rac1*$^{-/-}$ showing increased steady-state depression ($EPSC_{ss}$ / $EPSC_1$)
179 (Fig. 2A). Despite the stronger relative short-term depression, absolute steady-state EPSC
180 amplitudes were almost two-fold larger in *Rac1*$^{-/-}$ (*Rac1*$^{+/+}$ = 0.47 ± 0.14 nA vs.
181 *Rac1*$^{-/-}$ = 0.84 ± 0.22 nA, $p < 0.001$, n = 15/15, Fig. 2D1). At 500 Hz stimulation, *Rac1*$^{+/+}$ showed
182 robust short-term facilitation, which was absent in *Rac1*$^{-/-}$ (PPR: Rac1$^{+/+}$ = 1.2 ± 0.1 vs.
183 *Rac1*$^{-/-}$ = 1 ± 0.1, $p < 0.001$, n = 15/15, Fig. 2B). Similar to 50 Hz stimulation, *Rac1*$^{-/-}$ showed
184 more pronounced relative steady-state depression at 500 Hz stimulation. Notably, absolute
185 steady-state EPSC amplitudes at 500 Hz stimulation frequency were similar for *Rac1*$^{+/+}$ and
186 *Rac1*$^{-/-}$ (Fig. 2D1).
187 Since the loss of Rac1 increased synaptic strength and altered STP, we aimed to identify the
188 underlying mechanisms and evaluated RRP size and SV release probability (P_r) using
189 established quantal analysis methods (Elmqvist and Quastel, 1965; Neher, 2015; Thanawala
190 and Regehr, 2016). We estimated RRP size using 500 Hz stimulus trains which effectively
191 depleted the RRP in both *Rac1*$^{+/+}$ and *Rac1*$^{-/-}$ synapses by applying three conventional
192 paradigms based on the common assumption of quantal release originating from a single and
193 functionally homogenous pool of readily-releasable SVs (Neher, 2015; Schneggenburger and
194 Rosenmund, 2015): EQ, NpRf, and SMN with correction (Elmqvist and Quastel, 1965; Neher,
195 2015; Thanawala and Regehr, 2016). All three methods reported a moderate increase in RRP

196 size in *Rac1*$^{-/-}$ calyces (Fig. 2D2), however, this was statistically significant only for SMN
197 analysis. The initial P_r of resting synapses was estimated by dividing the $EPSC_1$ amplitude by
198 the estimated RRP sizes. All three analysis methods revealed an approximately two-fold
199 increase in P_r (SMN: *Rac1*$^{+/+}$ = 0.09 ± 0.02 vs. *Rac1*$^{-/-}$ = 0.15 ± 0.03, $p < 0.001$; NpRf:
200 *Rac1*$^{+/+}$ = 0.09 ± 0.02 vs. *Rac1*$^{-/-}$ = 0.17 ± 0.03, $p < 0.001$; EQ: *Rac1*$^{+/+}$ = 0.09 ± 0.02 vs.
201 *Rac1*$^{-/-}$ = 0.17 ± 0.04, $p < 0.001$, n = 15/15, Fig. 2D3). Therefore, based on the assumption of a
202 single and functionally homogenous RRP, this analysis indicates that presynaptic Rac1 deletion
203 increases synaptic strength and short-term depression primarily by elevating initial P_r with little
204 increase in RRP size. This suggests that Rac1 controls synaptic strength as a negative regulator
205 of P_r.

206 **Loss of Rac1 increases mEPSC frequency but not amplitude**

207 The RRP size and the P_r of the fusion-competent SVs is determined by the SV priming process,
208 which involves the assembly of the molecular fusion apparatus, defined as 'molecular priming'.
209 In addition, P_r also depends on the spatial coupling between docked SVs and Ca^{2+} entry sites
210 which may be adjusted by a distinct 'positional priming' step. Thus, 'molecular priming'
211 encompasses the steps that render SVs fusion competent and regulate their intrinsic
212 fusogenicity (Basu et al., 2007; Xue et al., 2010; Schneggenburger and Rosenmund, 2015;
213 Schotten et al., 2015), while positional priming consists of the steps that place molecularly
214 primed SVs close to voltage-gated calcium channels (VGCCs) (Neher, 2010). The spatial
215 coupling between SV and VGCCs critically determines the speed and efficacy of AP-evoked
216 release (Eggermann et al., 2012; Stanley, 2016). Spontaneous SV release is not or only little
217 dependent on VGCCs (Schneggenburger and Rosenmund, 2015; Kavalali, 2020), and the
218 frequency of miniature EPSC (mEPSCs) can, thus, be interpreted as a readout of intrinsic SV
219 fusogenicity at basal Ca^{2+} with increased SV fusogenicity causing higher mEPSC frequencies
220 (Basu et al., 2007; Schotten et al., 2015; Dong et al., 2018).Therefore, to determine if an
221 increased intrinsic SV fusogenicity caused the increase in P_r, we recorded mEPSCs from

222 *Rac1*$^{+/+}$ and *Rac1*$^{-/-}$ calyx synapses (Fig. 3) and found a four-fold increase in mEPSC frequency
223 (*Rac1*$^{+/+}$ = 3.4 ± 4.4 Hz vs. *Rac1*$^{-/-}$ = 14.3 ± 6.5 Hz, $p < 0.001$, n = 15/11) with no change in
224 mEPSC amplitude or waveform. To rule out that the increased mEPSC frequencies were due to
225 changes in presynaptic Ca^{2+} currents, we recorded mEPSCs in the presence of 200 µM Cd^{2+}, a
226 non-specific VGCC blocker. Since Cd^{2+} did not affect mEPSC frequencies we conclude that
227 Rac1 loss increases intrinsic SV fusogenicity at basal Ca^{2+}.

228 **Loss of Rac1 increases EPSC onset delays and decreases synchronicity of AP-evoked**
229 **release**

230 Although we found an increase in SV fusogenicity, this does not rule out an additional role for
231 Rac1 in regulating spatial coupling distances between molecularly primed SVs and VGCCs. In
232 the mature calyx of Held, AP-evoked SV release is governed by local Ca^{2+} nanodomains,
233 ensuring a fast onset and highly synchronous AP-evoked EPSCs to faithfully encode auditory
234 information (Fedchyshyn and Wang, 2005). In addition to the gating kinetics of presynaptic
235 VGCCs and postsynaptic AMPARs, the time between presynaptic AP and EPSC onset (EPSC
236 onset delay) is determined by the coupling distance between SVs and VGCCs. The coupling
237 distance defines the time for Ca^{2+} to diffuse and bind to the Ca^{2+} sensor and initiate SV fusion
238 (Fedchyshyn and Wang, 2007; Nakamura et al., 2015). Thus, EPSC onset delays can serve as
239 a readout of changes in spatial coupling distances, as increased onset delays are consistent
240 with SVs being more loosely coupled to VGCCs and vice versa. Therefore, we measured EPSC
241 onset delays during 50 Hz and 500 Hz stimulation (Fig. 4A, B) and found them to become
242 progressively larger during stimulation for *Rac1*$^{+/+}$ and *Rac1*$^{-/-}$ calyces. At 50 Hz, the increase in
243 EPSC onset delays during stimulus trains was comparable between *Rac1*$^{+/+}$ and *Rac1*$^{-/-}$,
244 amounting to about 60 µs between the first and the last ten EPSCs. At 500 Hz stimulation,
245 however, EPSC onset delays increased more rapidly in *Rac1*$^{-/-}$, with steady-state EPSC onset
246 delays being significantly larger for *Rac1*$^{-/-}$ compared to *Rac1*$^{+/+}$ (*Rac1*$^{+/+}$ = 94± 32 µs vs.
247 *Rac1*$^{-/-}$ = 131 ± 29 µs, $p = 0.004$, n = 15/15).

248 In addition to modulating EPSC onset delays, coupling distances between SV and
249 VGCCs affect the time course of synchronous release and the relative contribution of
250 synchronous versus asynchronous release during AP trains (Wadel et al., 2007; Chen et al.,
251 2015; Stanley, 2016; Yang et al., 2021). This is because synchronous release is dominated by
252 tightly coupled SVs which rapidly fuse in response to high local [Ca^{2+}], while asynchronous
253 release likely represents a stronger contribution of more loosely coupled SVs (Sakaba, 2006;
254 Schneggenburger and Rosenmund, 2015). An approximate measure for changes in the time
255 course of AP-evoked release can be obtained by analyzing the EPSC charge over EPSC
256 amplitude ratio ('effective EPSC duration') representing the width of a square current pulse with
257 same amplitude as the EPSC peak and same integral as the EPSC charge. Therefore, we
258 calculated the effective EPSC duration for both 50 Hz and 500 Hz stimulation (Fig. 4C) and
259 found its value for $EPSC_1$ comparable between *Rac1*$^{+/+}$ and *Rac1*$^{-/-}$. At steady-state during
260 50 Hz stimulation, however, the effective EPSC duration was slightly longer in *Rac1*$^{-/-}$
261 (*Rac1*$^{+/+}$ = 0.32 ± 0.03 ms vs. *Rac1*$^{-/-}$ = 0.35 ± 0.03 ms, $p = 0.006$). At steady-state during
262 500 Hz stimulation, the effective EPSC duration in *Rac1*$^{-/-}$ calyces was prolonged further and
263 increased by ~25% compared to *Rac1*$^{+/+}$ (*Rac1*$^{+/+}$ = 0.43 ± 0.04 ms vs.
264 *Rac1*$^{-/-}$ = 0.55 ± 0.12 ms, $p < 0.001$). These findings are consistent with transmitter release
265 being less synchronous in *Rac1*$^{-/-}$ synapses, especially during sustained activity at high AP
266 firing rates.

267 In summary, we found that *Rac1*$^{-/-}$ synapses had longer EPSC onset delays and showed
268 more strongly increasing effective EPSC durations during stimulus trains, especially at high
269 stimulation frequencies, implying less synchronous release. Since tighter SV to VGCCs coupling
270 has the opposite effect, i.e., generates shorter EPSC onset delays and more tightly
271 synchronized release, we conclude that the increase of synaptic strength in *Rac1*$^{-/-}$ calyces is
272 not due to tighter spatial coupling between SVs and VGCCs.

Loss of Rac1 facilitates EPSC recovery and RRP replenishment

The kinetics of molecular priming regulates RRP replenishment and determines steady-state release rates during high-frequency stimulation (Lipstein et al., 2013; Ritzau-Jost et al., 2018; Lipstein et al., 2021). Since *Rac1* deletion increased steady-state release during 50 Hz stimulus trains, we hypothesized that SV pool replenishment proceeds faster in the absence of Rac1. To test how Rac1 loss influences RRP replenishment, we applied afferent fiber stimulation using a paired train protocol consisting of a 500 Hz depleting train (50 APs) followed by a second 500 Hz test train at varying recovery intervals (Fig. 5). Recovery was then measured for both the initial EPSC amplitude and the RRP estimate of the test trains. Recovery of the initial EPSC amplitude was quantified in terms of both its absolute (Fig. 5A2) and its fractional value (Fig. 5A3), with the latter being the ratio ($EPSC_{test}$ − $EPSC_{ss}$) / ($EPSC_1$ − $EPSC_{ss}$), where $EPSC_{test}$, $EPSC_1$ and $EPSC_{ss}$ are the initial amplitude of the test train, and the first and the steady-state amplitudes of the 500 Hz conditioning train, respectively. Recovery of absolute $EPSC_1$ amplitude was significantly different between *Rac1*$^{+/+}$ and *Rac1*$^{-/-}$ (*Rac1*$^{+/+}$: A = 1.4, τ_{fast} = 17 ms, τ_{slow} = 2.7 s, f_{slow} = 0.67, τ_w = 1.8 s vs. *Rac1*$^{-/-}$: A = 3.4, τ_{fast} = 29 ms, τ_{slow} = 2.3 s, f_{slow} = 0.71, τ_w = 1.6 s, $p < 0.001$, n = 15/15) and fractional EPSC recovery was almost 50% faster in *Rac1*$^{-/-}$ (*Rac1*$^{+/+}$: τ_{fast} = 36 ms, τ_{slow} = 2.1 s, f_{slow} = 0.89, τ_w = 1.9 s vs. *Rac1*$^{-/-}$: τ_{fast} = 46 ms, τ_{slow} = 1.7 s, f_{slow} = 0.76, τ_w = 1.3 s, $p < 0.001$, Fig. 5A). Next, we analyzed fractional RRP recovery by dividing the RRP estimate of the test train by the RRP estimate of the depleting train and found that RRP recovery rates were about 40% faster in *Rac1*$^{-/-}$ (*Rac1*$^{+/+}$: τ_{fast} = 20 ms, τ_{slow} = 1.6 s, f_{slow} = 0.69, τ_w = 1.1 s vs. *Rac1*$^{-/-}$: τ_{fast} = 39 ms, τ_{slow} = 1.3 s, f_{slow} = 0.52, τ_w = 0.7 s, $p < 0.001$, Fig. 5B). Finally, we compared paired-pulse ratios ($EPSC_2$ / $EPSC_1$) at individual recovery intervals. Independent of recovery interval, PPR was consistently lower in *Rac1*$^{-/-}$ (*Rac1*$^{+/+}$ = 1.3 ± 0.1 vs. *Rac1*$^{-/-}$ = 1.1 ± 0.1, $p < 0.001$, Fig. 5C), consistent with an increase in P_r.

297 **Numerical simulations of STP and EPSC recovery are consistent with altered SV priming**
298 **after Rac1 loss**
299 Since the loss of presynaptic Rac1 caused three principal changes in synaptic function: (*i*)
300 increased synaptic strength (Fig. 2D1), (*ii*) increased steady-state release during 50 Hz
301 stimulation (Fig. 2A2), and (*iii*) accelerated EPSC recovery following conditioning 500 Hz trains
302 (Fig. 5), we next sought to corroborate our conclusions about underlying synaptic mechanisms
303 by reproducing experimental data in numerical simulations. To do so, we used two distinct STP
304 models: (1) a single pool model with a Ca^{2+}-dependent SV pool replenishment similar to the
305 release-site model of Weis et al. (1999) and (2) a recently established sequential two-step
306 priming scheme (Neher and Taschenberger, 2021; Lin et al., 2022).
307 The single-pool model assumes a single type of release site to which SVs can reversibly
308 dock, and SV docking and priming is described by a single transition step (Fig. 6A1). The
309 kinetics of the forward (priming) transition (determined by the rate constant k_f) is characterized
310 by a Michaelis-Menten-like dependence on cytosolic [Ca^{2+}] (Fig. 6A2 inset) while the backward
311 (unpriming) transition has a fixed rate constant (k_b). For resting synapses, the equilibrium
312 between empty sites (ES) and sites occupied by a docked and primed SV (DS) is given by the
313 ratio k_f/k_b at basal [Ca^{2+}] in this scheme. The total number of SV docking sites (N_{total}), priming
314 and unpriming rate constants (k_f and k_b), Ca-dependence of the priming step (parameters σ and
315 $K_{0.5}$), release probability P_r, and the time course of [Ca^{2+}] regulating the priming speed ('effective
316 [Ca^{2+}]') were free parameters and adjusted by trial and error (Fig. 6 – Figure supplement 1) to
317 reproduce experimentally observed differences in the time course of fractional recovery (Fig.
318 6A3), initial synaptic strength, and time course of STP during 50 and 500 Hz stimulation (Fig.
319 6A4). A comparison between simulated and experimental data shows that the single pool model
320 can describe the functional differences between *Rac1*$^{+/+}$ and *Rac1*$^{-/-}$ synapses, reproducing
321 larger initial synaptic strength, larger steady-state release during 50 Hz trains in Rac1-deficient
322 synapses, and similar steady-state release during 500 Hz trains in both genotypes (Fig. 6A5).

323 To describe both *Rac1*$^{+/+}$ and *Rac1*$^{-/-}$ synapses adequately, we had to introduce changes
324 in N_{total}, priming kinetics and P_r. The best fit was achieved by adjusting the ratio k_f/k_b at basal
325 [Ca^{2+}] to yield a number of release sites occupied with a docked/primed SV at rest (RRP) of
326 2150 and 2532 and by setting P_r to 0.08 and 0.165 for *Rac1*$^{+/+}$ and *Rac1*$^{-/-}$ synapses,
327 respectively (Fig. 6 – Figure supplement 1). Larger initial synaptic strength in *Rac1*$^{-/-}$ synapses
328 resulted from ~1.2 fold and ~2 fold changes in *RRP* and P_r, respectively, which is consistent with
329 the analysis shown in Fig. 2, which rests on similar assumptions as the single-pool STP model.
330 The higher steady state release in *Rac1*$^{-/-}$ synapses is primarily a result of their higher priming
331 rate constant k_1 for effective [Ca^{2+}] up to ~1 µM, while a faster saturation of k_1 with effective
332 [Ca^{2+}] above ~1 µM in *Rac1*$^{-/-}$ synapses (Fig. 6A2) accounts for steady-state release during
333 500 Hz stimulation being similar to *Rac1*$^{+/+}$ (Fig. 6A5).
334 Subsequently, we simulated our experimental data using a two-step priming scheme,
335 which postulates a sequential build-up of the SV fusion apparatus and distinguishes two distinct
336 priming states - an immature loosely-docked state (LS) and a mature tightly-docked (TS) state
337 (Neher and Brose, 2018; Neher and Taschenberger, 2021; Lin et al., 2022). The two-step
338 priming scheme (Fig. 6B1) reproduces functional changes in *Rac1*$^{-/-}$ synapses, including the
339 accelerated EPSC recovery after pool depletion (Fig. 6B3), increased initial EPSC amplitudes,
340 and elevated steady-state release during 50 Hz trains (Fig. 6B4). In contrast to simulations using
341 the single-pool model (Fig. 6A1), only the model parameters determining the SV priming kinetics
342 needed to be adjusted to reproduce the changes in *Rac1*$^{-/-}$ synapses when using the sequential
343 two-step model (Fig. 6B1). In resting *Rac1*$^{-/-}$ synapses, the priming equilibrium was shifted
344 towards a higher fraction of TS SVs in addition to a slight reduction of the fraction of empty sites
345 (ES) because of the increased priming rate constants k_1 and k_2 at resting cytosolic [Ca^{2+}]. The
346 higher abundance of fusion-competent SVs in resting *Rac1*$^{-/-}$ synapses (*Rac1*$^{+/+}$ = 691 TS SVs
347 vs. *Rac1*$^{-/-}$ = 1666 TS SVs) fully accounts for their increased synaptic strength, while the P_r and
348 the total number of sites N_{total} were constrained to the same values for *Rac1*$^{+/+}$ and *Rac1*$^{-/-}$

349 synapses. Proper adjustment of the Ca^{2+}-dependence of k_1 and k_2 (Fig. 6B2) reproduces the
350 different steady-state release in *Rac1*$^{-/-}$ compared to *Rac1*$^{+/+}$ synapses (Fig. 6B4). The steeper
351 increase in k_1 and k_2 with increasing [Ca^{2+}] (Fig. 6B2) accounts for the faster recovery early after
352 cessation of 500 Hz conditioning when [Ca^{2+}] is still elevated (Fig. 6B3). Thus, the sequential
353 two-step model is capable of replicating the observed changes in *Rac1*$^{-/-}$ synapses (Fig. 6B3,
354 6B5) solely by modifying the priming equilibrium between LS and TS SVs in resting synapses
355 and carefully adjusting the Ca^{2+}-dependence of the two SV priming steps with unaltered model
356 parameter values for P_r and N_{total}.

357 In summary, the experimental data available do not allow us to unambiguously favor one
358 model over the other (Fig. 6A1 vs. 6B1). Both models reproduce differences in STP and EPSC
359 recovery between *Rac1*$^{-/-}$ and *Rac1*$^{+/+}$ synapses, and both models require increased SV priming
360 speed at resting and intermediate [Ca^{2+}] in *Rac1*$^{-/-}$ synapses to reproduce the data faithfully.
361 While the single-pool model (Fig. 6A1) requires different values for N_{total} and P_r, to account for
362 the changes observed between *Rac1*$^{-/-}$ and *Rac1*$^{+/+}$ synapses, necessary changes to model
363 parameters were limited to those determining the SV priming equilibrium (k_1, b_1, k_2, b_2) when
364 using the sequential two-step model (Fig. 6B1).

365 **Loss of Rac1 impacts delay and temporal precision of AP firing in response to SAM**
366 **stimuli**

367 Animal vocalization, including human speech, is characterized by rapid amplitude modulations
368 (Joris et al., 2004). These amplitude modulations can be mimicked by sinusoidal amplitude-
369 modulated stimuli (SAM), which will produce periodic fluctuations in the firing rates of the calyx
370 of Held (Mc Laughlin et al., 2008; Tolnai et al., 2008). Therefore, different SAM frequencies will
371 differentially stress SV release and recovery mechanisms and can be used to reveal how the
372 observed changes in synaptic strength and SV pool recovery potentially impact auditory
373 signaling in *Rac1*$^{-/-}$ calyces. Using *in vivo* responses to SAM stimuli (Tolnai et al., 2008) which
374 contained modulation frequencies between 20 and 2000 Hz as templates for afferent fiber

375 stimulation, we recorded postsynaptic APs in the loose-patch configuration (Fig. 7). First, we
376 analyzed the success probability of presynaptic stimuli triggering a postsynaptic AP to assess
377 the reliability of synaptic transmission and found no difference between *Rac1*$^{+/+}$ and *Rac1*$^{-/-}$ for
378 all modulation frequencies tested (Fig. 7B1). Since temporal precision is crucial in auditory
379 signaling, we then analyzed if loss of Rac1 affected the temporal precision of AP generation by
380 calculating the standard deviation of AP delays ('AP jitter'). For all modulation frequencies,
381 temporal precision was unchanged when analyzed for the complete stimulus (Fig. 7B2).
382 However, our previous analysis showed that EPSC onset delay and synchronicity were only
383 affected at high stimulation frequencies. Since the SAM stimuli generate periods of high firing
384 activity interspersed with periods of low activity, we tested how preceding activity influenced AP
385 jitter and AP delay. First, we used the preceding inter-spike interval (ISI) to estimate preceding
386 activity and calculated AP jitter and AP delay for different ISIs (Fig. 7C1). Both AP jitter and AP
387 delay were comparable between *Rac1*$^{+/+}$ and *Rac1*$^{-/-}$ for most ISIs, but AP delay in *Rac1*$^{-/-}$
388 increased slightly at short ISIs. Previous studies showed that EPSC/EPSP amplitudes, and
389 subsequent AP generation, are influenced by preceding neuronal activity (Haustein et al., 2008;
390 Englitz et al., 2009; Lorteije et al., 2009; Sonntag et al., 2011; Yang and Xu-Friedman, 2015;
391 Ghanbari et al., 2020). Since the analysis shown in Fig. 7C1 only considered the last ISI, it may
392 result in an incomplete estimate of preceding activity. Therefore, we additionally estimated
393 activity levels by calculating the sum of all preceding APs weighted by their distance to the AP
394 under observation (Fig. 7C2). Using this approach, we found that AP jitter was similar in *Rac1*$^{+/+}$
395 and *Rac1*$^{-/-}$ synapses for low to moderate activity levels but diverged at increasing activity
396 levels, with *Rac1*$^{-/-}$ showing higher AP jitter (*Rac1*$^{+/+}$ = 65 ± 32 µs vs. *Rac1*$^{-/-}$ = 99 ± 62 µs,
397 $p < 0.001$, n = 14/18). Likewise, AP delays were similar for low activity levels but increased more
398 strongly in *Rac1*$^{-/-}$ with increasing activity (*Rac1*$^{+/+}$ = 110 ± 52 µs vs. *Rac1*$^{-/-}$ = 158 ± 101 µs,
399 $p = 0.03$). These data suggest that the activity-dependent increase in EPSC onset and reduction

400 in EPSC synchronicity in *Rac1*$^{-/-}$ at high stimulation frequencies translates into a small but
401 consistent increase in AP delays and AP jitter.
402

403 **Discussion**

404 By genetically ablating Rac1 at the calyx of Held after hearing onset, we identified presynaptic
405 roles of Rac1 in regulating synaptic transmission and plasticity in a native neuronal circuit.
406 Based on our experimental data and numerical simulations, we identify presynaptic Rac1 as a
407 key regulator of synaptic strength and SV pool replenishment by controlling SV priming kinetics
408 and, depending on model assumptions, by either regulating P_r (single-pool model) or by
409 regulating the abundance of tightly docked and fusion-competent SVs (sequential two-step
410 priming model). In conclusion, we propose that presynaptic Rac1 is a critical regulator for
411 encoding information flow in neuronal circuits.

412 **Presynaptic Rac1 regulates initial synaptic strength**

413 Our finding that Rac1 regulates initial synaptic strength contrasts with a recent study in primary
414 cultured hippocampal neurons which concluded that presynaptic Rac1 had no such effect
415 (O'Neil et al., 2021). Multiple reasons may explain these differences. One cause may be due to
416 the specific conditions of a native neuronal circuit which are not fully replicated under *in vitro*
417 conditions in cultured neuronal circuits. We specifically abated Rac1 at an advanced
418 developmental stage, two days after hearing onset, at which neuronal circuit properties are well
419 defined, and the calyx of Held is functionally largely mature (Englitz et al., 2009; Sonntag et al.,
420 2009; Sonntag et al., 2011; Borst and Soria van Hoeve, 2012). Although Rac1 was ablated at 10
421 days *in vitro* in the study by O'Neil et al. (2021), the corresponding developmental *in-vivo* stage
422 is difficult to estimate. In addition, it is unknown how and to what extent culture conditions
423 determine synaptic transmission and STP characteristics of hippocampal synapses developing
424 *in vitro*. Another critical difference between our study and that of O'Neil et al. (2021) was the
425 recording condition. We used 1.2 mM external [Ca^{2+}] and physiological temperature to mimic *in-*
426 *vivo* conditions (Lorteije et al., 2009; Borst, 2010; Forsberg et al., 2019), while O'Neil et al.
427 (2021) performed experiments at 2 mM external [Ca^{2+}] and room temperature. As a result, our
428 estimates for initial P_r based on the ratio of $EPSC_1$ over RRP had a mean of ~0.1 in *Rac1*$^{+/+}$

429 calyces, and values for individual synapses never exceeded 0.15, which allowed us to observe a
430 two-fold increase following Rac1 ablation. In the cultured neurons, using a similar analysis, a
431 mean initial P_r of ~0.4 was reported for *Rac1*$^{+/+}$ with values for individual synapses frequently
432 exceeding 0.5 in both excitatory and inhibitory neurons. It is therefore possible that in cultured
433 neurons, P_r was close to saturation, thereby occluding any further increase in initial synaptic
434 strength in *Rac1*$^{-/-}$ neurons. In addition, many regulatory steps in the SV cycle are temperature-
435 dependent (Chanaday and Kavalali, 2020), and in mouse hippocampal synapses, actin-
436 dependent synaptic release enhancement is restricted to physiological temperatures (Jensen et
437 al., 2007).

438 **Presynaptic Rac1 regulates SV pool replenishment**

439 The availability of fusion-competent SVs critically determines synaptic strength during ongoing
440 stimulation. The steady-state occupancy of the RRP varies with stimulation rates (Hallermann
441 and Silver, 2013; Neher, 2015) and is determined by the SV pool replenishment kinetics, which
442 are critical for maintaining synaptic transmission. Pool replenishment is typically quantified by
443 two methods (Hallermann and Silver, 2013; Neher, 2015): (1) the replenishment rate during
444 ongoing stimulation can be obtained as the slope of line fits to the steady-state portion of
445 cumulative EPSC trains assuming that during ongoing stimulation quantal release is balanced by
446 newly replenished SVs. (2) Replenishment rate constants after stimulation can be estimated
447 from the time constants of exponential fits to the time course of the fractional EPSC or pool
448 recovery plotted as a function of the inter-stimulus interval following conditioning trains.

449 We found that *Rac1*$^{-/-}$ calyces had larger steady-state EPSC amplitudes, and the slope
450 of the line fits to cumulative EPSC trains revealed a faster replenishment rate at 50 Hz
451 stimulation, similar to observations in hippocampal cultures at 20 and 40 Hz stimulation (O'Neil
452 et al., 2021). In contrast, during ongoing 500 Hz stimulation, steady-state EPSC amplitudes and
453 slope of the line fits were similar in *Rac1*$^{+/+}$ and *Rac1*$^{-/-}$ synapses. However, time courses of
454 EPSC or pool recovery after 500 Hz conditioning showed an almost 50% faster recovery when fit

455 by bi-exponential functions. This acceleration was largely due to a speed-up of τ_{slow} and a larger
456 contribution of τ_{fast}, which according to our simulations, reflects a faster recovery occurring at
457 cytosolic [Ca^{2+}] relatively close to resting values. In addition, we estimated a slightly larger
458 relative fraction of the fast recovery component in *Rac1*$^{-/-}$ synapses, which, according to our
459 simulations, reflects the magnitude of Ca-dependent acceleration of SV pool replenishment
460 immediately after cessation of 500 Hz conditioning while cytosolic [Ca^{2+}] decays back to resting
461 values. These observations are consistent with the experimental finding of an enhanced steady-
462 state release in *Rac1*$^{-/-}$ synapses during 50 Hz stimulation, which reflects their faster pool
463 replenishment at [Ca^{2+}] <1 μM because of the steeper increase of the forward priming rate
464 constants with increasing cytosolic [Ca^{2+}]. The steady-state release was similar during 500 Hz
465 trains when the synapses regenerate fusion-competent SVs at similar maximum rates in *Rac1*$^{+/+}$
466 and *Rac1*$^{-/-}$. This was primarily caused by a stronger saturation of the Ca-dependence of the
467 priming rate constant for [Ca^{2+}] >1 μM in *Rac1*$^{-/-}$synapses. Because of the similar steady-state
468 EPSC levels measured at 500 Hz, it is unlikely that Rac1 controls an upstream limit on the
469 priming process.

470 **Presynaptic Rac1 regulation of spontaneous release**

471 At mature calyx of Held synapse, blocking presynaptic Ca^{2+} influx through VGCCs does
472 not change spontaneous release rates (Dong et al., 2018). Thus, mEPSC frequencies can be
473 interpreted as a readout of intrinsic SV fusogenicity at basal [Ca^{2+}] with higher mEPSC
474 frequencies reflecting increased SV fusogenicity (Basu et al., 2007; Schotten et al., 2015; Dong
475 et al., 2018), provided that pool size remains unaltered. However, SVs undergoing AP-evoked
476 and spontaneous release may not necessarily originate from the same SV pools. Nevertheless,
477 all SVs have to undergo a priming step to acquire fusion competence. Actin is found throughout
478 the presynaptic terminal and application of latrunculin causes a rapid increase in mEPSCs rates
479 in the presence of internal Ca^{2+} chelators (BAPTA-AM, EGTA-AM) while also augmenting AP
480 evoked release (Morales et al., 2000). Thus, although Rac1 loss may differentially affect

481 mEPSCs rates and rates of AP-evoked release, increased mEPSC frequencies following Rac1
482 loss are consistent with a higher fusogenicity of those SVs contributing to spontaneous release
483 presumably due to Rac1's role as actin regulator.

484 **Presynaptic Rac1 does not affect the spatial coupling between docked SV and VGCCs**

485 After docking to release sites, SVs become fusion-competent during the assembly of the
486 molecular fusion machinery, which defines the intrinsic SV fusogenicity. In addition to the
487 intrinsic SV fusogenicity, the probability of SVs undergoing fusion upon AP arrival is determined
488 by their spatial coupling distances to VGCCs, which determines the local [Ca^{2+}] 'seen' by the
489 vesicular Ca^{2+} sensor for fusion (Neher, 2010; Schneggenburger and Rosenmund, 2015).
490 Therefore, the proximity of SVs to VGCCs (also termed 'positional priming') is a critical
491 determinant of transmitter release (Wadel et al., 2007; Chen et al., 2015; Stanley, 2016). At the
492 calyx of Held after hearing onset, AP-evoked SV release is controlled by local [Ca^{2+}]
493 nanodomains generated around $Ca_V2.1$ channels which are located at ~25 nm distance from
494 docked SVs (Fedchyshyn and Wang, 2005; Chen et al., 2015; Nakamura et al., 2015), resulting
495 in fast synchronous transmitter release. Since Rac1 regulates actin dynamics, loss of Rac1 may
496 result in tighter spatial coupling between SV and VGCCs, thereby increasing synaptic strength. If
497 SVs were located in closer proximity to VGCCs, we would expect to see decreased initial EPSC
498 onset delay times or decreased EPSC onset delay times during both 50 and 500 Hz stimulation.
499 However, we found that EPSCs in *Rac1*$^{-/-}$ calyx synapses had increased EPSC onset delays
500 and less synchronous EPSCs, particularly at high firing rates, which is inconsistent with SVs
501 being more tightly coupled to VGCCs.

502 The EPSC onset delay includes the AP conduction delay, the time between triggering an
503 AP by afferent fiber stimulation and its arrival at the calyx terminal, and the transmitter release
504 delay, the time between presynaptic AP and SV fusion which is dependent on the distance
505 between SVs to VGCCs (Fedchyshyn and Wang, 2007). Therefore, we cannot exclude that loss
506 of Rac1 may prolong conduction delay, thereby obscuring a role of Rac1 in regulating SV to

507 VGCC coupling distances. However, EPSC onset delays of the first EPSC or during 50 Hz train
508 stimuli were similar between *Rac1*$^{+/+-}$ and *Rac1*$^{-/-}$ calyces. The EPSC onset delay was only
509 increased for steady-state EPSCs during 500 Hz stimulation. In addition, if longer conduction
510 delays were solely responsible for the increase in EPSC onset delays, no changes in release
511 kinetics would be expected. However, during both 50 and 500 Hz stimulus trains, the effective
512 EPSC duration increased more strongly in *Rac1*$^{-/-}$ calyces compared to *Rac1*$^{+/+}$ consistent with
513 a less synchronized release time course in the former, possibly because of a larger fraction of
514 SVs located distally from VGCCs contributing to release in *Rac1*$^{-/-}$.

515 Another possibility is that presynaptic APs in *Rac1*$^{-/-}$ were broader and thereby increased
516 presynaptic Ca^{2+} influx which contributed to increased synaptic strength and faster EPSC
517 recovery. Although broader presynaptic APs are expected to widen the release transient and
518 may delay presynaptic Ca^{2+} influx occurring mainly during AP repolarization (Borst and
519 Sakmann, 1998; Li et al., 2007; Wang et al., 2008; Kochubey et al., 2009) and thereby increase
520 synaptic delays, we did not observe an increased effective EPSC duration or longer EPSC onset
521 delays between *Rac1*$^{+/+-}$ and *Rac1*$^{-/-}$ calyces for $EPSC_1$. Even though we cannot exclude a
522 Rac1-dependent regulation of presynaptic AP waveform, we do not consider such scenario very
523 likely. Using TEA, a Kv3 channel blocker, to broaden the presynaptic AP impairs high-frequency
524 firing at the calyx of Held (Wang et al., 1998; Wang and Kaczmarek, 1998; Johnston et al.,
525 2010). Since *Rac1*$^{-/-}$ calyces were able to follow high-frequency stimulation and EPSC onset
526 delays were similar for $EPSC_1$ and throughout the 50 Hz stimulus train it is unlikely loss of Rac1
527 caused a general broadening of APs. Therefore, in the absence of experimental evidence
528 supporting Rac1 loss-induced changes in SV to VGCC coupling distances, we propose that
529 Rac1 regulates synaptic strength and RRP recovery at the level of molecular priming, either by
530 increasing the intrinsic fusogenicity of SVs and their P_r or by increasing the abundance of fusion-
531 competent tightly docked SVs. In both scenarios, increased P_r *(*single pool model*)* or a shift in

532 priming equilibrium in favor of TS SVs (two-step model) could account for the increased initial
533 synaptic strength in *Rac1*$^{-/-}$ synapses and, at least in part, for their higher mEPSC rates.
534 Although our experimental data do not allow us to favor one scenario over the other
535 unambiguously, both models suggest that Rac1 regulates SV priming. While it was not required
536 to postulate differences in P_r when simulating *Rac1*$^{+/+-}$ and *Rac1*$^{-/-}$ synapse with a sequential
537 two-step model, we cannot rule out that P_r is indeed changed after Rac1 loss. It is well possible
538 to implement a higher P_r in *Rac1*$^{-/-}$ calyces within the framework of a sequential two-step model
539 and future experiments combined with simulations will be needed to explore this possibility
540 further.
541 Loss of Rac1 might also impact endocytosis through changes in actin signaling (Wu and
542 Chan, 2022). However, at the calyx of Held, the endocytic role of F-actin appears to be
543 negligible as actin depolymerization using latrunculin did not affect endocytosis (Eguchi et al.,
544 2017; Piriya Ananda Babu et al., 2020). Furthermore, endocytosis acts on a time scale of
545 seconds and would be too slow to affect SV pool replenishment during short stimulus trains
546 (Armbruster and Ryan, 2011). Although ultrafast endocytosis occurs on a timescale of tens of
547 milliseconds it is unlikely to contribute to the *Rac1*$^{-/-}$ phenotype as SV reformation is too slow
548 with a time scale of tens of seconds (Watanabe et al., 2013a; Watanabe et al., 2013b). In
549 addition, endocytosis is postulated to play a role in release site clearance (Neher, 2010; Sakaba
550 et al., 2013) as the perturbation of endocytosis increases the rate of synaptic depression and
551 slows RRP recovery (Wen et al., 2013) which we did not observe in the *Rac1*$^{-/-}$ calyces.

552 **Rac1 regulation of auditory signaling and information processing**

553 The ability to accurately encode sound information requires synaptic transmission in the lower
554 auditory brainstem to drive and sustain precise AP firing over rapid and large fluctuations of AP
555 firing rates up to the kilohertz range (Grothe et al., 2010; Borst and Soria van Hoeve, 2012;
556 Friauf et al., 2015). The calyx of Held - MNTB principal cell synapse is a failsafe and reliable
557 synaptic relay that transforms afferent AP spike patterns from the CN into precisely timed

558 inhibition to several mono- and binaural nuclei (Friauf and Ostwald, 1988; Spirou et al., 1990;
559 Joris et al., 2004; Englitz et al., 2009; Lorteije et al., 2009; Sonntag et al., 2011). The use of SAM
560 stimuli which mimics the neuronal response to environmental sounds (Joris et al., 2004; Tolnai
561 et al., 2008), suggests that loss of Rac1 did not deteriorate the faithful auditory signaling
562 properties over different amplitude modulation frequencies. However, we found that increased
563 EPSC onset and decreased SV release synchronicity in *Rac1*$^{-/-}$ translated into larger AP delay
564 and AP jitter at high activity levels. Although the absolute changes were modest, the need for
565 high temporal precision in the auditory brainstem might cause a more severe impact in
566 downstream nuclei, such as the lateral and medial superior olive. Since the calyx of Held
567 generates suprathreshold EPSPs even under short-term depression (Lorteije et al., 2009;
568 Lorteije and Borst, 2011), changes in synaptic strength caused by Rac1 ablation may affect
569 postsynaptic AP timing but should have little effect on postsynaptic AP firing success probability
570 in MNTB principal neurons. Synaptic transmission at other auditory synapses in the SPON,
571 MSO, or LSO that operate close to AP threshold or rely on synaptic integration to encode
572 information is likely more substantially affected by Rac1 ablation.

573 **Ideas and speculation**

574 **Rac1 regulation of F-actin dynamics controls SV priming**

575 F-actin regulates several SV cycle steps, which could impact SV replenishment rates (Morales et
576 al., 2000; Sakaba and Neher, 2003; Cingolani and Goda, 2008; Sun and Bamji, 2011; Waites et
577 al., 2011; Lee et al., 2012; Lee et al., 2013; Montesinos et al., 2015; Rust and Maritzen, 2015).
578 Specifically, F-actin may act as a physical barrier within the presynaptic AZ (Cingolani and
579 Goda, 2008) as the application of latrunculin transiently increases P_r and mEPSC rates (Morales
580 et al., 2000). Studies in which Septin 5 (Yang et al., 2010) or the actin cytoskeleton was
581 disrupted (Lee et al., 2012) are in support of the idea of F-actin as a structural barrier potentially
582 impacting molecular priming or SV to VGCC coupling (Yang et al., 2010). Assuming that SV
583 docking distance relative to the plasma membrane corresponds to SV priming (Imig et al., 2014;

584 Jung et al., 2016; Pulido and Marty, 2018), we propose that Rac1's regulation of F-actin may
585 impact the physical barrier and thus affect the conversion from LS to TS, although the P_r of the
586 final TS state in Rac1-deficient terminals remains unknown (Fig. 8). Based on our simulations,
587 we speculate that the loss of Rac1 results in local actin depolymerization in the AZ, thereby
588 promoting the LS to TS transition and/or increasing P_r of fusion-competent SVs by allowing
589 vesicle docking closer to the plasma membrane. In support of our model, increased synaptic
590 strength has been demonstrated to correlate with shortened tethering filaments that resulted in
591 SVs positioned more closely to the presynaptic membrane (Jung et al., 2021). It is also in line
592 with the finding that GIT proteins (Montesinos et al., 2015), Arp2/3 (O'Neil et al., 2021), and
593 Piccolo (Waites et al., 2011), which are all regulators of F-actin dynamics, also control synaptic
594 strength and suggests that molecules regulating F-actin dynamics at the AZ could be key
595 regulators of SV replenishment.

596 Mutations in Rac1 that result in loss or gain of function are associated with intellectual
597 disability (Reijnders et al., 2017; Zamboni et al., 2018). While much attention has focused on
598 Rac1 dysregulation in the dendritic compartment or the role of Rac1 in neuronal development,
599 our work demonstrates that presynaptic loss of Rac1 increases synaptic strength and EPSC
600 recovery independent of its developmental role. Human mutations of Rac1 may affect synaptic
601 strength at many different synaptic connections and potentially alter the excitation-inhibition
602 balance and synaptic information processing in neuronal circuits associated with neurological
603 disorders and addiction (Dietz et al., 2012; Bai et al., 2015; Wright et al., 2020).
604

605 **Methods**

Key Resources Table				
Reagent type (species) or resource	**Designation**	**Source or reference**	**Identifiers**	**Additional information**
strain, strain background (*Mus musculus*)	Rac1^{tm1Djk}/J (Rac1$^{flox/flox}$)	Jackson Laboratory (Glogauer et al., 2003)	RRID:IMSR_JAX:005550	either sex
antibody	anti-GFP (rabbit polyclonal)	Abcam	Cat# ab6556 RRID:AB_305564	EM (0.1 µg/mL)
antibody	6 nm colloidal Gold-AffiniPure anti-rabbit IgG (donkey polyclonal)	Jackson ImmunoResearch	Cat# 711-195-152 RRID:AB_2340609	EM (1:100)
sequence-based-reagent	primer: 5'-TCC AAT CTG TGC TGC CCA TC-3'	(Glogauer et al., 2003)		
sequence-based-reagent	primer: 5'-GAT GCT TCT AGG GGT GAG CC-3'	(Glogauer et al., 2003)		
recombinant DNA reagent	HdAd 28E4 hsyn iCre EGFP (viral vector)	Samuel M. Young, Jr., University of Iowa		
recombinant DNA reagent	HdAd 28E4 hsyn iCre mEGFP (viral vector)	Samuel M. Young, Jr., University of Iowa		
recombinant DNA reagent	HdAd 28E4 hsyn mEGFP (viral vector)	Samuel M. Young, Jr., University of Iowa		
chemical compound, drug	kynurenic acid	Tocris Bioscience	Cat# 0223	
chemical compound, drug	lidocaine N-ethyl bromide (QX-314)	Sigma Aldrich	Cat# L5783	
chemical compound, drug	D-AP5	Tocris Bioscience	Cat# 0106	
chemical compound, drug	(-)-bicuculline methochloride	Tocris Bioscience	Cat# 0131	
chemical compound, drug	strychnine hydrochloride	Tocris Bioscience	Cat# 2785	
chemical	tetraethylammonium	Sigma Aldrich	Cat# T-2265	

compound, drug	chloride			
chemical compound, drug	tetrodotoxin	Alomone labs	Cat# T-550	
chemical compound, drug	Cadmium chloride hemi(pentahydrate)	Sigma Aldrich	Cat# C3141	
software, algorithm	Matlab	The Mathworks	RRID:SCR_001622; v9.10	
software, algorithm	Patchmaster	HEKA; Harvard Bioscience	RRID:SCR_000034; v2x90.2	
software, algorithm	Igor Pro	Wavemetrics	RRID:SCR_000325; v6.37	
software, algorithm	Fiji	https://fiji.sc/	RRID:SCR_002285	
software, algorithm	Patcher's Power Tools	Max Planck Institute for Biophysical Chemistry; Gottingen; Germany	RRID:SCR_001950; v2.19	
software, algorithm	StereoDrive	Neurostar	N/A; v3.1.5	
software, algorithm	Live Acquisition	Thermo Fisher Scientific	N/A; v2.1.0.10	
software, algorithm	Neuromatic	(Rothman and Silver, 2018)	RRID:SCR_004186	

606

607 **Animals**

608 All experiments were performed following animal welfare laws and approved by the Institutional
609 Committee for Care and Use of Animals at the University of Iowa (PHS Assurance No. D16-
610 00009 (A3021-01) (Animal Protocol 0021952) and complied with accepted ethical best practices.
611 Animals were housed at a 12-hour light/dark cycle and had access to food and water ad libitum.
612 Experiments were performed on Rac1^{tm1Djk} (*Rac1*$^{fl/fl}$) mice (Glogauer et al., 2003)
613 (RRID:IMSR_JAX: 005550, The Jackson Laboratory, Bar Harbor, USA) of either sex. Animals of
614 this line possess a *loxP* site flanking exon 1 of the *Rac1* gene disrupting Rac1 expression after
615 recombination mediated by Cre recombinase. Genotyping was performed using PCR-
616 amplification with the following primers 5'-TCC AAT CTG TGC TGC CCA TC-3' and 5'-GAT
617 GCT TCT AGG GGT GAG CC-3' and amplification products (*Rac1*$^{fl/fl}$: 242 bp, wildtype: 115 bp)

618 were separated gel electrophoresis on a 1.5% agarose gel (Glogauer et al., 2003). Viral vectors
619 were injected at postnatal day 14 (P14) and experiments were performed at P28-30. All
620 available measures were taken to minimize animal pain and suffering.

621 **DNA construct and recombinant viral vector production**

622 Helper-dependent adenoviral vectors (HdAd) expressing a codon-optimized Cre recombinase
623 (Cre) (Shimshek et al., 2002) were produced as previously described (Montesinos et al., 2016;
624 Lubbert et al., 2017). These HdAd vectors contain two independent transgene cassettes that
625 independently express Cre recombinase and EGFP or myristoylated EGFP (mEGFP) under the
626 control of 470 bp human synapsin promoter (Lubbert et al., 2017). In brief, the expression
627 cassette with Cre recombinase was cloned into the pdelta28E4 SynEGFP plasmid using the
628 *Asc*I enzyme digestion site. The final plasmid has been modified to contain a separate EGFP or
629 myristoylated EGFP (mEGFP) expression cassette. Then, the pHAD plasmid was linearized by
630 *PmeI* enzyme to expose the ends of the 5' and 3' inverted terminal repeats (ITRs) and
631 transfected into 116 producer cells (Profection® Mammalian Transfection System, Promega,
632 Madison, WI, USA). Helper virus (HV) was added the following day for HdAd production. Forty-
633 eight hours postinfection, after cytopathic effects have taken place, cells were subjected to three
634 freeze/thaw cycles for lysis and release of the viral particles. HdAd was purified by CsCl
635 ultracentrifugation. HdAd was stored at -80 °C in storage buffer (10 mM HEPES, 1 mM $MgCl_2$,
636 250 mM sucrose, pH 7.4).

637 **Virus injections**

638 Virus injections at P14 were performed as previously described (Lubbert et al., 2019). Briefly,
639 mice were anesthetized with 5% isoflurane inhalation and anesthesia was maintained with 2%
640 isoflurane throughout the procedure. Subcutaneous injection of physiological saline, lidocaine,
641 bupivacaine, and meloxicam was used to treat loss of liquid and alleviate pain. The injection site
642 was determined using the Stereodrive software (Neurostar) and corrected for head orientation
643 and tilt. A small hole (diameter <1 mm) was drilled into the skull using a foot-pedal controlled drill

644 MH-170 (Foredom). The virus solution was injected via a glass pipet (Drummond) at a rate of
645 100 nL/min with a nanoliter injector (NanoW, Neurostar). Following the injection, the glass
646 needle was left in place for 1 min to dissipate the pressure and then slowly retracted. Animals
647 were then placed under an infrared heat lamp and allowed to recover before being returned to
648 their respective cages with their mother.

649 **Confocal imaging and reconstruction of presynaptic terminals**

650 For reconstruction of the calyx of Held terminals, animals were injected with viral vectors
651 expressing either mEGFP (yielding *Rac1*$^{+/+}$) or Cre recombinase and mEGFP (yielding *Rac1*$^{-/-}$).
652 Mice were anesthetized with an intraperitoneal injection of tribromoethanol (250 mg/kg body
653 weight) and transcardially perfused with ice-cold 0.1 M phosphate buffer (PB, pH 7.4) followed
654 by 4% paraformaldehyde (PFA) in 0.1 M PB. Brains were removed and post-fixed overnight in
655 4% PFA solution at 4°C. The next day, brains were sliced into 40 µm sections on a Leica
656 VT1200 vibratome. mEGFP positive slices were identified and mounted on cover slips with Aqua
657 Polymount (Polysciences, Inc., Warrington, PA, USA). Confocal images were acquired with a
658 Zeiss LSM 700 or 880 confocal scanning microscope using a 63x/1.3 NA Apochromat multi-
659 immersion objective. Image stacks were collected using 0.44 um plane line scans with line
660 average of four times. Images were processed using Fiji (Schindelin et al., 2012) (http://fiji.sc.,
661 RRID:SCR 002285). Calyx reconstructions were performed blind to genotype using Imaris
662 Measurement Pro (BitPlane) using automatic signal detection manual curation in single planes in
663 Z-stack confocal images as previously described (Radulovic et al., 2020).

664 **Electron microscopy**

665 Preembedding immuno-electron microscopy was performed as previously described
666 (Montesinos et al., 2015; Dong et al., 2018). Briefly, *Rac*$^{fl/fl}$ mice injected at P14 with HdAd co-
667 expressing Cre-recombinase and EGFP were anesthetized and perfused transcardially at P28
668 with phosphate-buffered saline (PBS, 150 mM NaCl, 25 mM Sørensen's phosphate buffer,
669 pH 7.4) followed by fixative solution for 7-9 min containing 4% PFA, 0.5% glutaraldehyde, and

670 0.2% picric acid in 100 mM Sørensen's phosphate buffer (PB, pH 7.4). Brains were post-fixed
671 with 4% PFA in PB overnight and 50-µm coronal sections of the brainstem were obtained on a
672 vibratome (Leica VT1200S). Expression of EGFP at the calyx of Held terminals was visualized
673 using an epifluorescence inverted microscope (CKX41, Olympus) equipped with an XCite Series
674 120Q lamp (Excelitas Technologies), and only those samples showing EGFP were further
675 processed. After washing with PB, sections were cryoprotected with 10%, 20%, and 30%
676 sucrose in PB, submersed into liquid nitrogen and then thawed. Sections were incubated in a
677 blocking solution containing 10% normal goat serum (NGS), 1% fish skin gelatin (FSG), in 50
678 mM Tris-buffered saline (TBS, 150 mM NaCl, 50 mM Tris, pH 7.4) for 1h, and incubated with an
679 anti-GFP antibody (0.1 µg/mL, ab6556, Abcam, RRID: AB_305564) diluted in TBS containing
680 1% NGS, 0.1% FSG plus 0.05% NaN_3 at 4°C for 48h. After washing with TBS, sections were
681 incubated overnight in nanogold conjugated donkey anti-rabbit IgG (1:100, Jackson
682 Immunoresearch, RRID: AB_2340609) diluted in TBS containing 1% NGS and 0.1% FSG.
683 Immunogold-labeled sections were washed in PBS, briefly fixed with 1% glutaraldehyde in PBS,
684 and silver intensified using an HQ silver intensification kit (Nanoprobe). After washing with PB,
685 sections were treated with 0.5% OsO_4 in 0.1 M PB for 20 min, en-bloc stained with 1% uranyl
686 acetate, dehydrated and flat embedded in Durcupan resin (Sigma-Aldrich). After trimming out
687 the MNTB region, ultrathin sections were prepared with 40 nm-thickness using an
688 ultramicrotome (EM UC7, Leica). Sections were counterstained with uranyl acetate and lead
689 citrate and examined in a Tecnai G2 Spirit BioTwin transmission electron microscope (Thermo
690 Fisher Scientific) at 100 kV acceleration voltage. Images were taken with a Veleta CCD camera
691 (Olympus) operated by TIA software (Thermo Fisher Scientific). Images used for quantification
692 were taken at 60 000x magnification.

693 **TEM image analysis**

694 Calyces positive for Cre expression (*Rac1*$^{-/-}$) were identified by immunogold labeling with an
695 anti-GFP antibody and compared to EGFP-negative terminals (*Rac1*$^{+/+}$) in the same slice or

696 calyces in the wildtype sample. All TEM data were analyzed using Fiji imaging analysis software
697 (Schindelin et al., 2012). Each presynaptic active zone (AZ) was defined as the membrane
698 directly opposing the postsynaptic density, and the length of each AZ was measured. Vesicles
699 within 200 nm from each AZ were manually selected and their distances relative to the AZ were
700 calculated using a 32-bit Euclidean distance map generated from the AZ. Synaptic vesicle
701 distances were binned every 5 nm and counted (Montesinos et al., 2015; Dong et al., 2018).
702 Vesicles less than 5 nm from the AZ were considered "docked". Three animals for each
703 condition and ~40 AZs per animal were analyzed. Three researchers performed analysis blind to
704 genotype independently and results were averaged.

705 **Electrophysiology**

706 Acute coronal brainstem slices (~200 µm) containing the MNTB were prepared as previously
707 described (Chen et al., 2013; Thomas et al., 2019). Briefly, after decapitation of the animal, the
708 brain was immersed in low-calcium artificial cerebrospinal fluid (aCSF) solution containing (in
709 mM): 125 NaCl, 2.5 KCl, 3 $MgCl_2$, 0.1 $CaCl_2$, 10 glucose, 25 $NaHCO_3$, 1.25 NaH_2PO_4, 0.4 L-
710 ascorbic acid, 3 myo-inositol, and 2 Na-pyruvate, pH 7.3–7.4). Brain slices were obtained using
711 a Leica VT 1200S vibratome equipped with zirconia ceramic blades (EF-INZ10, Cadence
712 Blades) as previously described. The blade was advanced at a speed of 20-50 µm/s. Slices
713 were immediately transferred to an incubation beaker containing standard extracellular solution
714 (same as above but using 1 mM $MgCl_2$ and 1.2 mM $CaCl_2$) at ~37°C and continuously bubbled
715 with 95% O_2–5% CO_2. After approximately 45 min of incubation, slices were transferred to a
716 recording chamber with the same saline solution at physiological temperature (~37°C).

717 Electrical stimulation of afferent fibers was performed as previously described (Forsythe and
718 Barnes-Davies, 1993). Briefly, a bipolar platinum-iridium electrode was positioned medially of the
719 MNTB to stimulate afferent fibers (FHC, Model MX214EP). Postsynaptic MNTB neurons were
720 whole-cell voltage-clamped at −60 mV using an EPC10/2 amplifier controlled by Patchmaster
721 Software (version 2x90.2, HEKA Elektronik, RRID:SCR_000034). Slices were continuously

722 perfused with standard aCSF solution at a rate of 1 mL/min and visualized by an upright
723 microscope (BX51WI, Olympus) through a 60x water-immersion objective (LUMPlanFL N,
724 Olympus) and an EMCCD camera (Andor Luca S, Oxford Instruments). To identify calyces
725 expressing Cre-recombinase and EGFP, the slice was illuminated at an excitation wavelength of
726 480 nm using a Polychrome V xenon bulb monochromator (TILL Photonics). For whole-cell
727 voltage-clamp recordings, the standard extracellular solution was supplemented with 1 mM
728 kynurenic acid to avoid saturation of postsynaptic AMPA receptors, 50 µM D-AP-5 to block
729 NMDA receptors, and 20 µM bicuculline and 5 µM strychnine to block inhibitory GABA- and
730 glycine receptors, respectively (all Tocris Bioscience). Patch pipettes had a resistance of ~3–4
731 MΩ and were filled with the following (in mM): 130 Cs-gluconate, 20 tetraethylammonium (TEA)-
732 Cl, 10 HEPES, 5 Na_2-phosphocreatine, 4 Mg-ATP, 0.3 Na-GTP, 6 QX-314, and 5 EGTA, pH 7.2
733 (315 mOsm. Reported voltages are uncorrected for a calculated liquid junction potential of 13
734 mV. For loose-patch recordings, the extracellular solution was supplemented with 20 µM
735 bicuculline and 5 µM strychnine, and the patch pipettes were filled with aCSF. To simulate *in*
736 *vivo* activity levels, afferent fibers were stimulated with activity patterns previously recorded *in*
737 *vivo* in response to sinusoidal amplitude-modulated (SAM) sound stimulation (Tolnai et al.,
738 2008).
739 mEPSCs were recorded with the same aCSF supplemented with 50 mM D-AP5, 20 µM
740 bicuculline, 5 µM strychnine, 1 µM TTX, and 20 mM TEA. In a subset of *Rac1*$^{-/-}$ recordings, Cd^{2+}
741 (cadmium chloride), a non-selective Ca^{2+} channel blocker was flushed in during recordings to
742 determine the impact of VGCC on spontaneous SV release. The baseline mEPSC frequency
743 was established by recording each cell for at least one minute before Cd^{2+} was flushed in via the
744 bath perfusion. MNTB principal neurons were whole-cell voltage-clamped at -80 mV and
745 recorded until enough mEPSCs (>25) were recorded. Overlapping events were excluded from
746 the analysis.

747 Data were acquired at a sampling rate of 100 kHz and lowpass filtered at 6 kHz. Series
748 resistance (3–8 MΩ) was compensated online to <3 MΩ, except for mEPSC recordings where
749 series resistance (<9 MΩ) was not compensated. All experiments were performed at near-
750 physiological temperature (36-37°C), and the temperature was maintained by a heated bath
751 chamber (HCS, ALA Scientific Instruments) and perfusion system (HPC-2, ALA Scientific
752 Instruments). The temperature of the bath solution was monitored during the experiment using a
753 glass-coated micro thermistor.

754 **Electrophysiological data analysis**

755 Electrophysiological data were imported to Matlab (version 9.10; The Mathworks,
756 RRID:SCR_001622) using a custom-modified version of sigTool (Lidierth, 2009) and Igor Pro
757 (version 8.0.4.2, Wavemetrics, RRID:SCR_000325) equipped with Patcher's Power Tools
758 (version 2.19, RRID:SCR_001950) and NeuroMatic (Rothman and Silver, 2018)
759 (RRID:SCR_004186), and analyzed offline with custom-written functions in Matlab and IgorPro.
760 The remaining series resistance was compensated offline to 0 MΩ with a time lag of 10 µs
761 (Traynelis, 1998). EPSC amplitudes were measured as peak amplitude minus baseline
762 preceding the EPSC. RRP size and P_r were calculated using the EQ method (Elmqvist and
763 Quastel, 1965), back-extrapolation method (SMN with correction) (Neher, 2015), and NpRf
764 model (Thanawala and Regehr, 2016) as previously described (Lubbert et al., 2019). Onset time
765 of EPSCs was determined by fitting a Boltzmann function to the EPSC rising flank and
766 calculating the time point of maximum curvature, as described previously (Fedchyshyn and
767 Wang, 2007). The duration between stimulus and EPSC onset was defined as EPSC onset
768 delay. The synchronicity of SV release for individual EPSCs was estimated from the effective
769 EPSC duration by dividing EPSC charge by EPSC amplitude. This 'effective EPSC duration'
770 indicates the width of a square current pulse with amplitude and charge identical to that of the
771 EPSC (Lopez-Murcia et al., 2019). A shorter 'effective width' indicates a shorter release transient
772 provided that mEPSC kinetics are unchanged.

773 Recordings of mEPSCs were analyzed using NeuroMatic in Igor Pro. Potential events were
774 detected when exceeding an amplitude threshold at 4-6 times the standard deviation of the
775 baseline and all events were manually curated to exclude false positives. Rise time was
776 measured between 10% and 90% of the peak amplitude.

777 Recovery of SVs was estimated by non-linear least-square fits to single EPSC and RRP
778 recovery time courses. Both types of recovery time courses were best fit with a bi-exponential
779 function of the form:

$$A\left(1-\left(f\left(e^{-\frac{t}{\tau_{d1}}}\right)+(1-f)\left(e^{-\frac{t}{\tau_{d2}}}\right)\right)\right)$$

780 with variable A constraint to 1 when fitting fractional recovery. An F-test was used to determine
781 the better fit. Fractional recovery of the first EPSC was calculated as $(EPSC_{test}^{1} - EPSC_{cond}^{ss})/$
782 $(EPSC_{cond}^{1} - EPSC_{cond}^{ss})$ where $EPSC_{test}^{1}$ is the amplitude of the first EPSC of the test train,
783 $EPSC_{cond}^{ss}$ the steady-state amplitude of the conditioning train and $EPSC_{cond}^{1}$ the amplitude of the
784 first EPSC of the conditioning train.

785 To estimate preceding neuronal activity during SAM stimulation, we calculated the interspike
786 interval (ISI) as the distance to the preceding AP. To analyze AP responses during SAM
787 stimulation, we used the preceding ISI to estimate the influence of previous activity during SAM
788 recordings. Since short-term plasticity can extend well beyond the last ISI, we also estimated
789 preceding activity by calculating the sum of all preceding events, with each event weighted by its
790 distance to the AP under observation. This weighting was implemented as a single-exponential
791 decaying function, emphasizing temporally close events over more distant ones (Sonntag et al.,
792 2011; Keine et al., 2016). The time constant was set to 30 ms, consistent with previous reports
793 (Yang and Xu-Friedman, 2015). The calculation was also performed with time constants of
794 10 ms and 100 ms yielding similar results.

795 **Experimental design and statistical analysis**

796 Individual neurons were considered independent samples for electrophysiological data analysis
797 and morphological reconstruction. For thin-section TEM analysis, AZs were considered
798 independent samples (244 total AZs, 6 animals, ~40 AZs each). Statistical analysis was
799 conducted in MATLAB (version 9.4, RRID:SCR_001622) and GraphPad Prism
800 (RRID:SCR_002798). Data distributions were tested for Gaussianity using the Shapiro-Wilk test.
801 To compare two groups, we used a two-tailed unpaired Student's t-test with Welch's correction
802 (normal distribution) or a two-tailed Mann-Whitney *U* test (non-normal distribution). An RM
803 ANOVA was performed to compare more than two groups with within-subject factors, and p-
804 values were Bonferroni-adjusted for multiple comparisons. Fits to data were subject to F-tests to
805 determine the better model (mono- or biexponential) and for comparison between groups. A p-
806 value of 0.05 was deemed significant for interpreting all statistical tests. Effect sizes were
807 calculated using the MES toolbox in MATLAB (Hentschke and Stuttgen, 2011) and are reported
808 as Cohen's U_1 for two-sample comparison and eta-squared (η^2) for RM ANOVA. No statistical
809 test was performed to pre-determine sample sizes. Exact p-values, test statistics, and effect
810 sizes for all statistical comparisons are summarized in supplemental tables. Boxplots show
811 median, interquartile, and minimum/maximum within 1.5 times the interquartile range. Average
812 data in the text are reported as mean ± standard deviation.

813 **Numerical simulations of STP and EPSC recovery**

814 Simulations of synaptic STP in response to 50 and 500 Hz stimulus trains and of the recovery of
815 EPSC amplitudes after SV pool depletion were performed using two types of kinetics schemes
816 for SV priming and fusion: (*i*) a simple single pool model with a Ca^{2+}-dependent SV pool
817 replenishment as described below, and (*ii*) the sequential two-step model as recently proposed
818 by Lin et al. (2022).

819 *Single pool model*

820 The simple single pool model consisted of a single type of release site to which SVs can
821 reversibly dock. The total number of sites (N_{total}) is, therefore, given at any given time point *t* by
822 the sum of empty release sites (N_e(t)) and the release sites occupied by a primed and fusion-
823 competent SV (N_o(t)): $N_{tot} = N_e(t) + N_o(t)$.

824 Transitions between N_e(t) and N_o(t) are described by forward (k_f) and backward (k_b) rate
825 constants according to:

$$\frac{d}{dt} N_o(t) = k_f \cdot N_e(t) - k_b \cdot N_o(t)$$

$$\frac{d}{dt} N_e(t) = k_b \cdot N_o(t) - k_f \cdot N_e(t)$$

826 While the backward (unpriming) rate constant had a fixed value, k_f was assumed to increase
827 with increasing cytosolic [Ca^{2+}] ('effective [Ca^{2+}]'). The Ca-dependence of k_f was described by a
828 Michaelis-Menten like saturation according to:

$$k_f(t) = \left(k_{f,rest} + \sigma \cdot ([Ca^{2+}](t) - [Ca^{2+}]_{rest})\right) / \left(1 + ([Ca^{2+}](t) - [Ca^{2+}]_{rest})/K_{0.5)}\right)$$

829 where $k_{f,rest}$ is the value of k_f at resting [Ca^{2+}] ([Ca^{2+}]$_{rest}$; assumed to be 50 nM), σ is a slope
830 factor and $K_{0.5}$ is the Michaelis-Menten K_D value.

831 The effective [Ca^{2+}] ([Ca^{2+}](t)) was assumed to increase instantaneously at action potential (AP)
832 arrival and to decay back to its resting value [Ca^{2+}]$_{rest}$ with a rate constant k_{Ca} according to the
833 rate equation:

$$\frac{d}{dt} [Ca^{2+}](t) = -k_{Ca} \cdot ([Ca^{2+}](t) - [Ca^{2+}]_{rest})$$

834 Release probability (P_r) at arrival of the jth AP was modelled according to

$$P_{r,j} = P_{r,1} \cdot {y_j}^{4.5} \cdot z_j$$

835 with y≥1 and z≤1. Here, $P_{r,1}$ designates the release probability for the first EPSC in a train, y_j
836 accounts for changes in local [Ca^{2+}] during repetitive stimulation ($y_j = [Ca^{2+}]_j/[Ca^{2+}]_1$), likely

837 due to presynaptic Ca^{2+} current facilitation, and/or saturation of local Ca^{2+} buffers, and *z*
838 accounts for a small reduction of P_r during repetitive stimulation.
839 Both variables y_j and z_j were initialized to 1 at the onset of a stimulus train. The variable *y* was
840 incremented after each AP by

$$y_{inc} = y_{inc,1} \cdot (y_{max} - y_j)$$

841 and *z* was decremented by

$$z_{dec} = z_{dec,1} \cdot (z_j - z_{min})$$

842 During inter-stimulus intervals, time courses of *y(t)* and *z(t)* were determined by the rate
843 equations:

$$\frac{d}{dt}\, y(t) = (1 - y(t)) \cdot k_y$$

$$\frac{d}{dt}\, z(t) = (1 - z(t)) \cdot k_z$$

844 (for details see Lin et al. (2022)).
845 For each release event, the quantal content m_j of the $EPSC_j$ triggered by stimulus *j* was
846 calculated as the product of $P_{r,j} \cdot N_o(t_j)$ with both quantities evaluated immediately before
847 stimulus arrival. Between APs, the differential equations were solved numerically using the fifth-
848 order Runge-Kutta-Fehlberg algorithm implemented in IgorPro (Wavemetrics). All model
849 parameters on the time course of effective [Ca^{2+}] and P_r during stimulus trains were constrained
850 to the same values for both genotypes. The remaining model parameters (N_{total}, initial P_r, k_f, k_b,
851 σ, $K_{0.5}$) were adjusted by trial and error to reproduce experimentally observed differences
852 between *Rac1*$^{+/+}$ and *Rac1*$^{-/-}$ synapses (Figure 6 figure supplement 1). The total number of SV
853 docking sites (N_{total}), priming and unpriming rate constants, Ca^{2+}-dependence of the priming
854 step, and P_r were free parameters and adjusted by trial and error to reproduce experimental data
855 on 1) the time course of fractional recovery after 500 Hz conditioning stimuli (Fig. 6A3), 2) initial
856 synaptic strength, and 3) the time course of STP during 50 and 500 Hz stimulation (Fig. 6A4).

857 *Sequential two-step model*

858 The sequential two-step model was implemented as previously described (Lin et al., 2022), with
859 the standard model parameters modified to reproduce experimentally observed STP and EPSC
860 recovery after conditioning trains in >P28 mouse calyx synapses and at physiological
861 temperature. All model parameters defining the time course of effective [Ca^{2+}] and P_r during
862 stimulus trains were constrained to the same values for both genotypes. Except for initial P_r and
863 N_{total}, the remaining model parameters were adjusted by trial and error to reproduce
864 experimentally observed differences between *Rac1*$^{+/+}$ and *Rac1*$^{-/-}$ synapses. Thus, only those
865 parameters determining the SV state transitions (k_1, b_1, σ_1, $K_{0.5}$, k_2, b_2, σ_2) were allowed to differ
866 between *Rac1*$^{+/+}$ and *Rac1*$^{-/-}$ synapses while initial P_r and N_{total} identical for both genotypes
867 (Figure 6 - figure supplement 2).

868

869 **Data and software accessibility**

870 All numerical data used to generate the figures are part of the respective source files.
871 Experimental raw data and custom-written software central to the conclusion of this study are
872 available at http://dx.doi.org/10.17632/c4b7gn8bh7 under the Creative Commons Attribution 4.0
873 License (CC BY 4.0).

Acknowledgments

We would like to thank the members of the Young lab for their comments on the manuscript.

Competing interests

The authors declare no competing interests.

878 **References**

879 Alabi AA, Tsien RW (2012) Synaptic vesicle pools and dynamics. Cold Spring Harbor
880 perspectives in biology 4:a013680.
881 Armbruster M, Ryan TA (2011) Synaptic vesicle retrieval time is a cell-wide rather than
882 individual-synapse property. Nat Neurosci 14:824-826.
883 Azarfar A, Calcini N, Huang C, Zeldenrust F, Celikel T (2018) Neural coding: A single neuron's
884 perspective. Neurosci Biobehav Rev 94:238-247.
885 Bai Y, Xiang X, Liang C, Shi L (2015) Regulating Rac in the nervous system: molecular function
886 and disease implication of Rac GEFs and GAPs. Biomed Res Int 2015:632450.
887 Basu J, Betz A, Brose N, Rosenmund C (2007) Munc13-1 C1 domain activation lowers the
888 energy barrier for synaptic vesicle fusion. J Neurosci 27:1200-1210.
889 Bleckert A, Photowala H, Alford S (2012) Dual pools of actin at presynaptic terminals. Journal of
890 neurophysiology 107:3479-3492.
891 Bonnycastle K, Davenport EC, Cousin MA (2021) Presynaptic dysfunction in
892 neurodevelopmental disorders: Insights from the synaptic vesicle life cycle. J Neurochem
893 157:179-207.
894 Borst JG (2010) The low synaptic release probability in vivo. Trends in neurosciences 33:259-
895 266.
896 Borst JG, Sakmann B (1998) Calcium current during a single action potential in a large
897 presynaptic terminal of the rat brainstem. J Physiol 506:143-157.
898 Borst JG, Soria van Hoeve J (2012) The calyx of held synapse: from model synapse to auditory
899 relay. Annual review of physiology 74:199-224.
900 Bosco EE, Mulloy JC, Zheng Y (2009) Rac1 GTPase: a "Rac" of all trades. Cell Mol Life Sci
901 66:370-374.
902 Brette R (2015) Philosophy of the Spike: Rate-Based vs. Spike-Based Theories of the Brain.
903 Front Syst Neurosci 9:151.
904 Chanaday NL, Kavalali ET (2020) Is Ca(2+) Essential for Synaptic Vesicle Endocytosis? Trends
905 in neurosciences 43:77-79.
906 Chen Z, Cooper B, Kalla S, Varoqueaux F, Young SM, Jr. (2013) The Munc13 proteins
907 differentially regulate readily releasable pool dynamics and calcium-dependent recovery
908 at a central synapse. The Journal of neuroscience : the official journal of the Society for
909 Neuroscience 33:8336-8351.
910 Chen Z, Das B, Nakamura Y, DiGregorio DA, Young SM, Jr. (2015) Ca2+ channel to synaptic
911 vesicle distance accounts for the readily releasable pool kinetics at a functionally mature
912 auditory synapse. J Neurosci 35:2083-2100.
913 Cingolani LA, Goda Y (2008) Actin in action: the interplay between the actin cytoskeleton and
914 synaptic efficacy. Nat Rev Neurosci 9:344-356.
915 Cole JC, Villa BR, Wilkinson RS (2000) Disruption of actin impedes transmitter release in snake
916 motor terminals. The Journal of physiology 525 Pt 3:579-586.
917 Crins TT, Rusu SI, Rodriguez-Contreras A, Borst JG (2011) Developmental changes in short-
918 term plasticity at the rat calyx of Held synapse. The Journal of neuroscience : the official
919 journal of the Society for Neuroscience 31:11706-11717.
920 Dietz DM et al. (2012) Rac1 is essential in cocaine-induced structural plasticity of nucleus
921 accumbens neurons. Nat Neurosci 15:891-896.
922 Dong W, Radulovic T, Goral RO, Thomas C, Suarez Montesinos M, Guerrero-Given D,
923 Hagiwara A, Putzke T, Hida Y, Abe M, Sakimura K, Kamasawa N, Ohtsuka T, Young
924 SM, Jr. (2018) CAST/ELKS Proteins Control Voltage-Gated Ca(2+) Channel Density and
925 Synaptic Release Probability at a Mammalian Central Synapse. Cell Rep 24:284-293
926 e286.

927 Doussau F, Gasman S, Humeau Y, Vitiello F, Popoff M, Boquet P, Bader MF, Poulain B (2000)
928 A Rho-related GTPase is involved in Ca(2+)-dependent neurotransmitter exocytosis. J
929 Biol Chem 275:7764-7770.
930 Eggermann E, Bucurenciu I, Goswami SP, Jonas P (2012) Nanodomain coupling between
931 Ca(2)(+) channels and sensors of exocytosis at fast mammalian synapses. Nat Rev
932 Neurosci 13:7-21.
933 Eguchi K, Taoufiq Z, Thorn-Seshold O, Trauner D, Hasegawa M, Takahashi T (2017) Wild-Type
934 Monomeric alpha-Synuclein Can Impair Vesicle Endocytosis and Synaptic Fidelity via
935 Tubulin Polymerization at the Calyx of Held. J Neurosci 37:6043-6052.
936 Elmqvist D, Quastel DM (1965) A quantitative study of end-plate potentials in isolated human
937 muscle. The Journal of physiology 178:505-529.
938 Englitz B, Tolnai S, Typlt M, Jost J, Rubsamen R (2009) Reliability of synaptic transmission at
939 the synapses of Held in vivo under acoustic stimulation. PLoS One 4:e7014.
940 Fedchyshyn MJ, Wang LY (2005) Developmental transformation of the release modality at the
941 calyx of Held synapse. The Journal of neuroscience : the official journal of the Society for
942 Neuroscience 25:4131-4140.
943 Fedchyshyn MJ, Wang LY (2007) Activity-dependent changes in temporal components of
944 neurotransmission at the juvenile mouse calyx of Held synapse. The Journal of
945 physiology 581:581-602.
946 Forsberg M, Seth H, Bjorefeldt A, Lyckenvik T, Andersson M, Wasling P, Zetterberg H, Hanse E
947 (2019) Ionized calcium in human cerebrospinal fluid and its influence on intrinsic and
948 synaptic excitability of hippocampal pyramidal neurons in the rat. J Neurochem 149:452-
949 470.
950 Forsythe ID, Barnes-Davies M (1993) The binaural auditory pathway: excitatory amino acid
951 receptors mediate dual timecourse excitatory postsynaptic currents in the rat medial
952 nucleus of the trapezoid body. Proc Biol Sci 251:151-157.
953 Friauf E, Ostwald J (1988) Divergent projections of physiologically characterized rat ventral
954 cochlear nucleus neurons as shown by intra-axonal injection of horseradish peroxidase.
955 Experimental brain research Experimentelle Hirnforschung Experimentation cerebrale
956 73:263-284.
957 Friauf E, Fischer AU, Fuhr MF (2015) Synaptic plasticity in the auditory system: a review. Cell
958 Tissue Res 361:177-213.
959 Gentile JE, Carrizales MG, Koleske AJ (2022) Control of Synapse Structure and Function by
960 Actin and Its Regulators. Cells 11.
961 Ghanbari A, Ren N, Keine C, Stoelzel C, Englitz B, Swadlow HA, Stevenson IH (2020) Modeling
962 the Short-Term Dynamics of in Vivo Excitatory Spike Transmission. J Neurosci 40:4185-
963 4202.
964 Glogauer M, Marchal CC, Zhu F, Worku A, Clausen BE, Foerster I, Marks P, Downey GP,
965 Dinauer M, Kwiatkowski DJ (2003) Rac1 deletion in mouse neutrophils has selective
966 effects on neutrophil functions. J Immunol 170:5652-5657.
967 Grothe B, Pecka M, McAlpine D (2010) Mechanisms of sound localization in mammals.
968 Physiological reviews 90:983-1012.
969 Hallermann S, Silver RA (2013) Sustaining rapid vesicular release at active zones: potential
970 roles for vesicle tethering. Trends in neurosciences 36:185-194.
971 Haustein MD, Reinert T, Warnatsch A, Englitz B, Dietz B, Robitzki A, Rubsamen R, Milenkovic I
972 (2008) Synaptic transmission and short-term plasticity at the calyx of Held synapse
973 revealed by multielectrode array recordings. J Neurosci Methods 174:227-236.
974 Hentschke H, Stuttgen MC (2011) Computation of measures of effect size for neuroscience data
975 sets. The European journal of neuroscience 34:1887-1894.

976 Imig C, Min SW, Krinner S, Arancillo M, Rosenmund C, Sudhof TC, Rhee J, Brose N, Cooper
977 BH (2014) The morphological and molecular nature of synaptic vesicle priming at
978 presynaptic active zones. Neuron 84:416-431.
979 Iwasaki S, Takahashi T (1998) Developmental changes in calcium channel types mediating
980 synaptic transmission in rat auditory brainstem. The Journal of physiology 509 (Pt
981 2):419-423.
982 Iwasaki S, Takahashi T (2001) Developmental regulation of transmitter release at the calyx of
983 Held in rat auditory brainstem. The Journal of physiology 534:861-871.
984 Iwasaki S, Momiyama A, Uchitel OD, Takahashi T (2000) Developmental changes in calcium
985 channel types mediating central synaptic transmission. J Neurosci 20:59-65.
986 Jensen V, Walaas SI, Hilfiker S, Ruiz A, Hvalby O (2007) A delayed response enhancement
987 during hippocampal presynaptic plasticity in mice. The Journal of physiology 583:129-
988 143.
989 Johnston J, Forsythe ID, Kopp-Scheinpflug C (2010) Going native: voltage-gated potassium
990 channels controlling neuronal excitability. The Journal of physiology 588:3187-3200.
991 Joris PX, Trussell LO (2018) The Calyx of Held: A Hypothesis on the Need for Reliable Timing in
992 an Intensity-Difference Encoder. Neuron 100:534-549.
993 Joris PX, Schreiner CE, Rees A (2004) Neural processing of amplitude-modulated sounds.
994 Physiological reviews 84:541-577.
995 Jung JH, Szule JA, Marshall RM, McMahan UJ (2016) Variable priming of a docked synaptic
996 vesicle. Proc Natl Acad Sci U S A 113:E1098-1107.
997 Jung JH, Kirk LM, Bourne JN, Harris KM (2021) Shortened tethering filaments stabilize
998 presynaptic vesicles in support of elevated release probability during LTP in rat
999 hippocampus. Proc Natl Acad Sci U S A 118.
1000 Kavalali ET (2020) Neuronal Ca(2+) signalling at rest and during spontaneous
1001 neurotransmission. The Journal of physiology 598:1649-1654.
1002 Keine C, Rubsamen R, Englitz B (2016) Inhibition in the auditory brainstem enhances signal
1003 representation and regulates gain in complex acoustic environments. Elife 5.
1004 Klug A, Borst JG, Carlson BA, Kopp-Scheinpflug C, Klyachko VA, Xu-Friedman MA (2012) How
1005 do short-term changes at synapses fine-tune information processing? J Neurosci
1006 32:14058-14063.
1007 Kochubey O, Han Y, Schneggenburger R (2009) Developmental regulation of the intracellular
1008 Ca^{2+} sensitivity of vesicle fusion and Ca^{2+}-secretion coupling at the rat calyx of Held. J
1009 Physiol 587:3009-3023.
1010 Kumanogoh H, Miyata S, Sokawa Y, Maekawa S (2001) Biochemical and morphological
1011 analysis on the localization of Rac1 in neurons. Neurosci Res 39:189-196.
1012 Lee JS, Ho WK, Lee SH (2012) Actin-dependent rapid recruitment of reluctant synaptic vesicles
1013 into a fast-releasing vesicle pool. Proceedings of the National Academy of Sciences of
1014 the United States of America 109:E765-774.
1015 Lee JS, Ho WK, Neher E, Lee SH (2013) Superpriming of synaptic vesicles after their
1016 recruitment to the readily releasable pool. Proceedings of the National Academy of
1017 Sciences of the United States of America 110:15079-15084.
1018 Li L, Bischofberger J, Jonas P (2007) Differential gating and recruitment of P/Q-, N-, and R-type
1019 Ca^{2+} channels in hippocampal mossy fiber boutons. J Neurosci 27:13420-13429.
1020 Lidierth M (2009) sigTOOL: A MATLAB-based environment for sharing laboratory-developed
1021 software to analyze biological signals. J Neurosci Methods 178:188-196.
1022 Lin KH, Taschenberger H, Neher E (2022) A sequential two-step priming scheme reproduces
1023 diversity in synaptic strength and short-term plasticity. Proc Natl Acad Sci U S A
1024 119:e2207987119.
1025 Lipstein N, Chang S, Lin KH, Lopez-Murcia FJ, Neher E, Taschenberger H, Brose N (2021)
1026 Munc13-1 is a Ca^{2+}-phospholipid-dependent vesicle priming hub that shapes synaptic

1027 short-term plasticity and enables sustained neurotransmission. Neuron 109:3980-4000
1028 e3987.
1029 Lipstein N, Sakaba T, Cooper BH, Lin KH, Strenzke N, Ashery U, Rhee JS, Taschenberger H,
1030 Neher E, Brose N (2013) Dynamic control of synaptic vesicle replenishment and short-
1031 term plasticity by Ca^{2+}-calmodulin-Munc13-1 signaling. Neuron 79:82-96.
1032 Lopez-Murcia FJ, Reim K, Jahn O, Taschenberger H, Brose N (2019) Acute Complexin
1033 Knockout Abates Spontaneous and Evoked Transmitter Release. Cell Rep 26:2521-2530
1034 e2525.
1035 Lorteije JA, Borst JG (2011) Contribution of the mouse calyx of Held synapse to tone adaptation.
1036 The European journal of neuroscience 33:251-258.
1037 Lorteije JA, Rusu SI, Kushmerick C, Borst JG (2009) Reliability and precision of the mouse calyx
1038 of Held synapse. The Journal of neuroscience : the official journal of the Society for
1039 Neuroscience 29:13770-13784.
1040 Lubbert M, Goral RO, Satterfield R, Putzke T, van den Maagdenberg AM, Kamasawa N, Young
1041 SM, Jr. (2017) A novel region in the CaV2.1 alpha1 subunit C-terminus regulates fast
1042 synaptic vesicle fusion and vesicle docking at the mammalian presynaptic active zone.
1043 Elife 6.
1044 Lubbert M, Goral RO, Keine C, Thomas C, Guerrero-Given D, Putzke T, Satterfield R,
1045 Kamasawa N, Young SM, Jr. (2019) CaV2.1 alpha1 Subunit Expression Regulates
1046 Presynaptic CaV2.1 Abundance and Synaptic Strength at a Central Synapse. Neuron
1047 101:260-273 e266.
1048 Mc Laughlin M, van der Heijden M, Joris PX (2008) How secure is in vivo synaptic transmission
1049 at the calyx of Held? The Journal of neuroscience : the official journal of the Society for
1050 Neuroscience 28:10206-10219.
1051 Miki T, Malagon G, Pulido C, Llano I, Neher E, Marty A (2016) Actin- and Myosin-Dependent
1052 Vesicle Loading of Presynaptic Docking Sites Prior to Exocytosis. Neuron 91:808-823.
1053 Montesinos MS, Satterfield R, Young SM, Jr. (2016) Helper-Dependent Adenoviral Vectors and
1054 Their Use for Neuroscience Applications. Methods Mol Biol 1474:73-90.
1055 Montesinos MS, Dong W, Goff K, Das B, Guerrero-Given D, Schmalzigaug R, Premont RT,
1056 Satterfield R, Kamasawa N, Young SM, Jr. (2015) Presynaptic Deletion of GIT Proteins
1057 Results in Increased Synaptic Strength at a Mammalian Central Synapse. Neuron
1058 88:918-925.
1059 Morales M, Colicos MA, Goda Y (2000) Actin-dependent regulation of neurotransmitter release
1060 at central synapses. Neuron 27:539-550.
1061 Nakamura Y, Harada H, Kamasawa N, Matsui K, Rothman JS, Shigemoto R, Silver RA,
1062 DiGregorio DA, Takahashi T (2015) Nanoscale distribution of presynaptic Ca(2+)
1063 channels and its impact on vesicular release during development. Neuron 85:145-158.
1064 Neher E (2010) What is Rate-Limiting during Sustained Synaptic Activity: Vesicle Supply or the
1065 Availability of Release Sites. Frontiers in synaptic neuroscience 2:144.
1066 Neher E (2015) Merits and Limitations of Vesicle Pool Models in View of Heterogeneous
1067 Populations of Synaptic Vesicles. Neuron 87:1131-1142.
1068 Neher E, Sakaba T (2008) Multiple roles of calcium ions in the regulation of neurotransmitter
1069 release. Neuron 59:861-872.
1070 Neher E, Brose N (2018) Dynamically Primed Synaptic Vesicle States: Key to Understand
1071 Synaptic Short-Term Plasticity. Neuron 100:1283-1291.
1072 Neher E, Taschenberger H (2021) Non-negative Matrix Factorization as a Tool to Distinguish
1073 Between Synaptic Vesicles in Different Functional States. Neuroscience 458:182-202.
1074 O'Neil SD, Racz B, Brown WE, Gao Y, Soderblom EJ, Yasuda R, Soderling SH (2021) Action
1075 potential-coupled Rho GTPase signaling drives presynaptic plasticity. Elife 10.

1076 Piriya Ananda Babu L, Wang HY, Eguchi K, Guillaud L, Takahashi T (2020) Microtubule and
1077 Actin Differentially Regulate Synaptic Vesicle Cycling to Maintain High-Frequency
1078 Neurotransmission. J Neurosci 40:131-142.
1079 Pulido C, Marty A (2018) A two-step docking site model predicting different short-term synaptic
1080 plasticity patterns. J Gen Physiol 150:1107-1124.
1081 Radulovic T, Dong W, Goral RO, Thomas CI, Veeraraghavan P, Montesinos MS, Guerrero-
1082 Given D, Goff K, Lubbert M, Kamasawa N, Ohtsuka T, Young SM, Jr. (2020) Presynaptic
1083 development is controlled by the core active zone proteins CAST/ELKS. The Journal of
1084 physiology 598:2431-2452.
1085 Reijnders MRF et al. (2017) RAC1 Missense Mutations in Developmental Disorders with Diverse
1086 Phenotypes. Am J Hum Genet 101:466-477.
1087 Reinagel P, Laughlin S (2001) Natural stimulus statistics. Network 12:237-240.
1088 Ritzau-Jost A, Jablonski L, Viotti J, Lipstein N, Eilers J, Hallermann S (2018) Apparent calcium
1089 dependence of vesicle recruitment. The Journal of physiology 596:4693-4707.
1090 Rollenhagen A, Lubke JH (2006) The morphology of excitatory central synapses: from structure
1091 to function. Cell Tissue Res 326:221-237.
1092 Rothman JS, Silver RA (2018) NeuroMatic: An Integrated Open-Source Software Toolkit for
1093 Acquisition, Analysis and Simulation of Electrophysiological Data. Front Neuroinform
1094 12:14.
1095 Rust MB, Maritzen T (2015) Relevance of presynaptic actin dynamics for synapse function and
1096 mouse behavior. Experimental cell research.
1097 Sakaba T (2006) Roles of the fast-releasing and the slowly releasing vesicles in synaptic
1098 transmission at the calyx of Held. J Neurosci 26:5863-5871.
1099 Sakaba T, Neher E (2003) Involvement of actin polymerization in vesicle recruitment at the calyx
1100 of Held synapse. The Journal of neuroscience : the official journal of the Society for
1101 Neuroscience 23:837-846.
1102 Sakaba T, Kononenko NL, Bacetic J, Pechstein A, Schmoranzer J, Yao L, Barth H, Shupliakov
1103 O, Kobler O, Aktories K, Haucke V (2013) Fast neurotransmitter release regulated by the
1104 endocytic scaffold intersectin. Proc Natl Acad Sci U S A 110:8266-8271.
1105 Satzler K, Sohl LF, Bollmann JH, Borst JG, Frotscher M, Sakmann B, Lubke JH (2002) Three-
1106 dimensional reconstruction of a calyx of Held and its postsynaptic principal neuron in the
1107 medial nucleus of the trapezoid body. The Journal of neuroscience : the official journal of
1108 the Society for Neuroscience 22:10567-10579.
1109 Schindelin J, Arganda-Carreras I, Frise E, Kaynig V, Longair M, Pietzsch T, Preibisch S, Rueden
1110 C, Saalfeld S, Schmid B, Tinevez JY, White DJ, Hartenstein V, Eliceiri K, Tomancak P,
1111 Cardona A (2012) Fiji: an open-source platform for biological-image analysis. Nature
1112 methods 9:676-682.
1113 Schneggenburger R, Rosenmund C (2015) Molecular mechanisms governing Ca(2+) regulation
1114 of evoked and spontaneous release. Nat Neurosci 18:935-941.
1115 Schotten S, Meijer M, Walter AM, Huson V, Mamer L, Kalogreades L, ter Veer M, Ruiter M,
1116 Brose N, Rosenmund C, Sorensen JB, Verhage M, Cornelisse LN (2015) Additive effects
1117 on the energy barrier for synaptic vesicle fusion cause supralinear effects on the vesicle
1118 fusion rate. Elife 4:e05531.
1119 Shimshek DR, Kim J, Hubner MR, Spergel DJ, Buchholz F, Casanova E, Stewart AF, Seeburg
1120 PH, Sprengel R (2002) Codon-improved Cre recombinase (iCre) expression in the
1121 mouse. Genesis 32:19-26.
1122 Sonntag M, Englitz B, Kopp-Scheinpflug C, Rubsamen R (2009) Early postnatal development of
1123 spontaneous and acoustically evoked discharge activity of principal cells of the medial
1124 nucleus of the trapezoid body: an in vivo study in mice. The Journal of neuroscience : the
1125 official journal of the Society for Neuroscience 29:9510-9520.

1126 Sonntag M, Englitz B, Typlt M, Rubsamen R (2011) The calyx of held develops adult-like
1127 dynamics and reliability by hearing onset in the mouse in vivo. The Journal of
1128 neuroscience : the official journal of the Society for Neuroscience 31:6699-6709.
1129 Spirou GA, Brownell WE, Zidanic M (1990) Recordings from cat trapezoid body and HRP
1130 labeling of globular bushy cell axons. Journal of neurophysiology 63:1169-1190.
1131 Stanley EF (2016) The Nanophysiology of Fast Transmitter Release. Trends in neurosciences
1132 39:183-197.
1133 Sun Y, Bamji SX (2011) beta-Pix modulates actin-mediated recruitment of synaptic vesicles to
1134 synapses. The Journal of neuroscience : the official journal of the Society for
1135 Neuroscience 31:17123-17133.
1136 Taschenberger H, Leao RM, Rowland KC, Spirou GA, von Gersdorff H (2002) Optimizing
1137 synaptic architecture and efficiency for high-frequency transmission. Neuron 36:1127-
1138 1143.
1139 Thanawala MS, Regehr WG (2016) Determining synaptic parameters using high-frequency
1140 activation. J Neurosci Methods 264:136-152.
1141 Theunissen FE, Elie JE (2014) Neural processing of natural sounds. Nat Rev Neurosci 15:355-
1142 366.
1143 Thomas CI, Keine C, Okayama S, Satterfield R, Musgrove M, Guerrero-Given D, Kamasawa N,
1144 Young SM, Jr. (2019) Presynaptic Mitochondria Volume and Abundance Increase during
1145 Development of a High-Fidelity Synapse. J Neurosci 39:7994-8012.
1146 Threadgill R, Bobb K, Ghosh A (1997) Regulation of dendritic growth and remodeling by Rho,
1147 Rac, and Cdc42. Neuron 19:625-634.
1148 Tolnai S, Hernandez O, Englitz B, Rubsamen R, Malmierca MS (2008) The medial nucleus of
1149 the trapezoid body in rat: spectral and temporal properties vary with anatomical location
1150 of the units. The European journal of neuroscience 27:2587-2598.
1151 Torres VI, Vallejo D, Inestrosa NC (2017) Emerging Synaptic Molecules as Candidates in the
1152 Etiology of Neurological Disorders. Neural Plast 2017:8081758.
1153 Traynelis SF (1998) Software-based correction of single compartment series resistance errors. J
1154 Neurosci Methods 86:25-34.
1155 Wadel K, Neher E, Sakaba T (2007) The coupling between synaptic vesicles and Ca2+
1156 channels determines fast neurotransmitter release. Neuron 53:563-575.
1157 Waites CL, Leal-Ortiz SA, Andlauer TF, Sigrist SJ, Garner CC (2011) Piccolo regulates the
1158 dynamic assembly of presynaptic F-actin. The Journal of neuroscience : the official
1159 journal of the Society for Neuroscience 31:14250-14263.
1160 Wang LY, Kaczmarek LK (1998) High-frequency firing helps replenish the readily releasable
1161 pool of synaptic vesicles. Nature 394:384-388.
1162 Wang LY, Neher E, Taschenberger H (2008) Synaptic vesicles in mature calyx of Held synapses
1163 sense higher nanodomain calcium concentrations during action potential-evoked
1164 glutamate release. J Neurosci 28:14450-14458.
1165 Wang LY, Gan L, Forsythe ID, Kaczmarek LK (1998) Contribution of the Kv3.1 potassium
1166 channel to high-frequency firing in mouse auditory neurones. The Journal of physiology
1167 509 (Pt 1):183-194.
1168 Watanabe S, Liu Q, Davis MW, Hollopeter G, Thomas N, Jorgensen NB, Jorgensen EM (2013a)
1169 Ultrafast endocytosis at Caenorhabditis elegans neuromuscular junctions. Elife
1170 2:e00723.
1171 Watanabe S, Rost BR, Camacho-Perez M, Davis MW, Sohl-Kielczynski B, Rosenmund C,
1172 Jorgensen EM (2013b) Ultrafast endocytosis at mouse hippocampal synapses. Nature
1173 504:242-247.
1174 Weis S, Schneggenburger R, Neher E (1999) Properties of a model of Ca^{++}-dependent vesicle
1175 pool dynamics and short term synaptic depression. Biophys J 77:2418-2429.

1176 Wen H, Hubbard JM, Rakela B, Linhoff MW, Mandel G, Brehm P (2013) Synchronous and
1177 asynchronous modes of synaptic transmission utilize different calcium sources. Elife
1178 2:e01206.
1179 Wimmer VC, Horstmann H, Groh A, Kuner T (2006) Donut-like topology of synaptic vesicles with
1180 a central cluster of mitochondria wrapped into membrane protrusions: a novel structure-
1181 function module of the adult calyx of Held. The Journal of neuroscience : the official
1182 journal of the Society for Neuroscience 26:109-116.
1183 Wondolowski J, Dickman D (2013) Emerging links between homeostatic synaptic plasticity and
1184 neurological disease. Front Cell Neurosci 7:223.
1185 Wright WJ, Graziane NM, Neumann PA, Hamilton PJ, Cates HM, Fuerst L, Spenceley A,
1186 MacKinnon-Booth N, Iyer K, Huang YH, Shaham Y, Schluter OM, Nestler EJ, Dong Y
1187 (2020) Silent synapses dictate cocaine memory destabilization and reconsolidation. Nat
1188 Neurosci 23:32-46.
1189 Wu LG, Chan CY (2022) Multiple Roles of Actin in Exo- and Endocytosis. Frontiers in synaptic
1190 neuroscience 14:841704.
1191 Xu Z, Chen Y, Chen Y (2019) Spatiotemporal Regulation of Rho GTPases in Neuronal
1192 Migration. Cells 8.
1193 Xue M, Craig TK, Xu J, Chao HT, Rizo J, Rosenmund C (2010) Binding of the complexin N
1194 terminus to the SNARE complex potentiates synaptic-vesicle fusogenicity. Nat Struct Mol
1195 Biol 17:568-575.
1196 Yang CH, Ho WK, Lee SH (2021) Postnatal maturation of glutamate clearance and release
1197 kinetics at the rat and mouse calyx of Held synapses. Synapse 75:e22215.
1198 Yang H, Xu-Friedman MA (2015) Skipped-stimulus approach reveals that short-term plasticity
1199 dominates synaptic strength during ongoing activity. J Neurosci 35:8297-8307.
1200 Yang YM, Fedchyshyn MJ, Grande G, Aitoubah J, Tsang CW, Xie H, Ackerley CA, Trimble WS,
1201 Wang LY (2010) Septins regulate developmental switching from microdomain to
1202 nanodomain coupling of Ca(2+) influx to neurotransmitter release at a central synapse.
1203 Neuron 67:100-115.
1204 Yasuda R (2017) Biophysics of Biochemical Signaling in Dendritic Spines: Implications in
1205 Synaptic Plasticity. Biophys J 113:2152-2159.
1206 Young SM, Jr., Neher E (2009) Synaptotagmin has an essential function in synaptic vesicle
1207 positioning for synchronous release in addition to its role as a calcium sensor. Neuron
1208 63:482-496.
1209 Zamboni V, Jones R, Umbach A, Ammoni A, Passafaro M, Hirsch E, Merlo GR (2018) Rho
1210 GTPases in Intellectual Disability: From Genetics to Therapeutic Opportunities. Int J Mol
1211 Sci 19.
1212 Zhang H, Ben Zablah Y, Zhang H, Jia Z (2021) Rho Signaling in Synaptic Plasticity, Memory,
1213 and Brain Disorders. Front Cell Dev Biol 9:729076.
1214

1215

1216 **Figures legends**

1217 **Fig. 1: Loss of presynaptic Rac1 after hearing onset does not affect calyx of Held gross**
1218 **morphology or ultrastructure**. (**A**) Cre recombinase-expressing HdAds were injected into the
1219 cochlear nucleus of *Rac1*$^{fl/fl}$ mice at P14, yielding *Rac1*$^{-/-}$ calyces of Held. All experiments were
1220 performed at around four weeks of age. Cre-recombinase-expressing calyces could be visually
1221 identified by simultaneous expression of EGFP. (**B1**) Representative reconstruction of calyx
1222 terminals of *Rac1*$^{+/+}$ (left) and *Rac1*$^{-/-}$ (right) animals. (**B2**) Calyx morphology assessed by
1223 surface area (left) and volume (right) was not affected by the loss of Rac1. (**C1**) Representative
1224 EM images of the active zone (yellow) and docked SV (blue) to assess synaptic ultrastructure.
1225 (**C2**) AZ length and number of docked SV were comparable between *Rac1*$^{+/+}$ *and Rac1*$^{-/-}$. (**C3**)
1226 SV distribution as a function of distance to AZ was not different between *Rac1*$^{+/+}$ and *Rac1*$^{-/-}$.
1227 Box plot whiskers extend to the minimum/maximum within the 1.5 interquartile range; open
1228 markers indicate individual data points. For EM data, the results of three independent
1229 investigators were averaged. All data shown in the figure and the detailed results of statistical
1230 tests are part of the supplementary file.

1231 **Figure 1 – source data 1:** Excel file containing the data shown in Figure 1 and the results of
1232 statistical analysis.

1233

1234 **Fig. 2: Presynaptic Rac1 regulates synaptic vesicles release probability and synaptic**
1235 **strength.** Synaptic transmission at the calyx of Held – MNTB synapse was studied at P28 after
1236 deletion of Rac1 at P14 at different stimulation frequencies. (**A1, B1**) Representative evoked
1237 EPSCs for *Rac1*$^{+/+}$ (black) and *Rac1*$^{-/-}$ (orange) at 50 Hz and 500 Hz stimulation frequency.
1238 Stimulus artifacts were blanked for clarity. (**C**) Magnification of the first EPSC. Ablation of
1239 presynaptic Rac1 resulted in increased EPSC amplitude with no change in EPSC dynamics.
1240 (**A2-A4**) At 50 Hz stimulation frequency, *Rac1*$^{-/-}$ showed stronger short-term depression and
1241 larger steady-state EPSC amplitudes. (**B2-B4**) At 500 Hz stimulation frequency, loss of Rac1

1242 resulted in a lack of short-term facilitation and increased synaptic depression with no change in
1243 steady-state EPSC amplitude. (**D1**) Population data showing an increase in first EPSC amplitude
1244 in *Rac1*$^{-/-}$. Steady-state EPSC amplitudes were increased in *Rac1*$^{-/-}$ at 50 Hz but not at 500 Hz
1245 stimulation frequency. (**D2**) Population data of RRP using three different estimation methods,
1246 suggesting little to no change in RRP size (**D3**) Population data indicating that release probability
1247 in *Rac1*$^{-/-}$ was elevated independent of estimation method. All data shown in the figure and the
1248 detailed results of statistical tests are part of the supplementary file.
1249 **Figure 2 – source data 1:** Excel file containing the data shown in Figure 2 and the results of
1250 statistical analysis.
1251
1252 **Fig. 3: Presynaptic loss of Rac1 increase calcium-independent neurotransmitter release.**
1253 (**A**) Representative recordings of mEPSCs for *Rac1*$^{+/+}$ (left, black) and *Rac1*$^{-/-}$ (right, orange).
1254 (**B1-B4**) Rac1 deletion increased mEPSC frequency but did not affect mEPSC amplitude, rise
1255 time, or full width at half-maximal amplitude (FWHM). (**C**) The increased mEPSC rates at
1256 *Rac1*$^{-/-}$ were independent of presynaptic voltage-gated calcium channels (VGCC), as blocking
1257 VGCC with cadmium (Cd^{2+}) did not affect mEPSC frequency. All data shown in the figure and
1258 the detailed results of statistical tests are part of the supplementary file.
1259 **Figure 3 – source data 1:** Excel file containing the data shown in Figure 3 and the results of
1260 statistical analysis.
1261
1262 **Fig. 4: Presynaptic loss of Rac1 decreases SV synchronicity and prolongs EPSC onset at**
1263 **high-frequency stimulation.** (**A**) Experiments were performed at low (50 Hz, A1) and high
1264 (500 Hz, A2) stimulation frequencies. Representative recordings of first ($EPSC_1$) and last
1265 ($EPSC_{50}$) EPSC in the stimulus train. Traces are aligned at the EPSC onset of the first EPSC.
1266 Stimulus artifacts are partially blanked for better visibility. Note the shift in the onset of $EPSC_{50}$ in
1267 *Rac1*$^{-/-}$ compared to *Rac1*$^{+/+}$ at 500 Hz but not 50 Hz. (**B1**) Absolute EPSC onset delay for
1268 50 Hz (gray and light orange) and 500 Hz (black and orange) stimulation. (**B2**) EPSC onset

1269 delay relative to $EPSC_1$ for 50 Hz (gray and light orange) and 500 Hz (black and orange). At
1270 50 Hz, the EPSC onset delay was similar between *Rac1*$^{+/+}$ and *Rac1*$^{-/-}$. At 500 Hz, the EPSC
1271 onset delay was substantially larger at *Rac1*$^{-/-}$. For better visualization, only every second data
1272 point is shown. (**B3**) EPSC onset delay of the last ten EPSCs relative to $EPSC_1$ for 50 Hz and
1273 500 Hz stimulation. EPSC delay of the last ten EPSC was not different between *Rac1*$^{+/+}$ and
1274 *Rac1*$^{-/-}$ at 50 Hz but increased for *Rac1*$^{-/-}$ at 500 Hz stimulation frequency. (**C1**) Analysis of
1275 'effective EPSC duration' to estimate SV release synchronicity during 50 Hz and 500 Hz
1276 stimulation. Synchronicity was estimated from 'effective EPSC duration' by dividing the EPSC
1277 charge by the EPSC amplitude. Note the increase in effective EPSC duration for *Rac1*$^{-/-}$ at
1278 500 Hz stimulation. For better visualization, only every second data point is shown (**C2**) EPSC
1279 duration was not different for $EPSC_1$ but slightly longer for late EPSCs in *Rac1*$^{-/-}$ at 50 Hz and
1280 substantially longer at 500 Hz stimulation frequency. (**C3**) EPSC duration of the last ten EPSCs
1281 normalized to $EPSC_1$. Note the progressive increase in EPSC duration in *Rac1*$^{-/-}$ with increasing
1282 stimulation frequency. All data shown in the figure and the detailed results of statistical tests are
1283 part of the supplementary file.
1284 **Figure 4 – source data 1:** Excel file containing the data shown in Figure 4 and the results of
1285 statistical analysis.
1286
1287 **Fig. 5: Loss of presynaptic Rac1 facilitates synaptic vesicle recovery**. Recovery of single
1288 EPSC and RRP recovery was measured by two consecutive train stimuli (conditioning stimulus
1289 and recovery stimulus) at 500 Hz at varying recovery intervals. (**A**) Single EPSC recovery. (**A1**)
1290 Representative traces for *Rac1*$^{+/+}$ (black) and *Rac1*$^{-/-}$ (orange) for recovery intervals ranging
1291 from 20 ms to 16 s. (**A2**) Recovery of absolute EPSC amplitudes as a function of recovery
1292 interval with a magnification of short intervals (right). (**A3**) Fractional EPSC recovery as a
1293 function of recovery interval. (**B**) Recovery of the RRP (**B1**) Representative recovery traces
1294 following a 100 ms and 2 s recovery interval. The depleting stimulus train is the same as in A1.

1295 (**B2**) Fractional RRP recovery was faster in *Rac1*$^{-/-}$ compared to *Rac1*$^{+/+}$. (**C**) Recovery of the
1296 paired-pulse ratio (PPR) of the first two EPSCs of the recovery train. PPR was consistently lower
1297 in *Rac1*$^{-/-}$, but the difference was emphasized at longer recovery intervals. All data shown in the
1298 figure and the detailed results of statistical tests are part of the supplementary file.
1299 **Figure 5 – source data 1:** Excel file containing the data shown in Figure 5 and the results of
1300 statistical analysis.
1301
1302 **Fig. 6: Numerical simulations of 50 and 500 Hz STP and EPSC recovery after conditioning**
1303 **500 Hz trains are consistent with *Rac1*-loss induced changes in SV priming.**
1304 Experimental observations were equally well reproduced by either of two kinetic schemes of SV
1305 priming and fusion: a single pool model (**A**) or a recently proposed (Lin et al., 2022) sequential
1306 two-step SV priming scheme (**B**). (**A1**) Diagram of vesicle states for the single pool model. SVs
1307 reversibly dock at empty release sites (ES). SVs in the docked and primed state (DS) undergo
1308 fusion with the probability P_r upon AP arrival. Vacated sites become immediately available for
1309 SV docking and priming. Transitions represented by dashed lines occur instantaneously, while
1310 those represented by solid lines occur with rate constants as indicated. Forward transition rate
1311 constant is Ca^{2+}-dependent. For the single pool model, P_r, and total number of sites (N_{total}) were
1312 free parameters for both genotypes. The model predicts an increased P_r from 0.08 (*Rac1*$^{+/+}$) to
1313 0.165 (*Rac1*$^{-/-}$) and an increase in the number of docked SVs (RRP) from 2150 SVs (*Rac1*$^{+/+}$) to
1314 2532 SVs (*Rac1*$^{-/-}$). (**A2**) Dependence of k_f on cytosolic [Ca^{2+}] (effective [Ca^{2+}]) for *Rac1*$^{+/+}$
1315 (black) and *Rac1*$^{-/-}$ (orange) synapses. The inset illustrates the time course of the effective
1316 [Ca^{2+}] during a 500 Hz train consisting of 40 stimuli. (**A3**) Predictions of the single pool model
1317 (lines) for the time course of the fractional recovery of $EPSC_{test}$ after 500 Hz conditioning trains
1318 superimposed onto experimental data for *Rac1*$^{+/+}$ (black circles) and *Rac1*$^{-/-}$ (orange triangles)
1319 synapses (data from Fig. 5A3). (**A4**) Predictions of the single pool model (lines) for the time
1320 course of STP during 50 Hz and 500 Hz trains superimposed onto experimental data (circles) for

1321 *Rac1*$^{+/+}$ (black, top panel) and *Rac1*$^{-/-}$ (orange, bottom panel) synapses. (**A5**) Model predictions
1322 for the time course of STP during 50 Hz and 500 Hz trains for *Rac1*$^{+/+}$ (gray and black) and
1323 *Rac1*$^{-/-}$ (light and dark orange) synapses shown superimposed to facilitate comparison. (**B1**)
1324 Diagram of vesicle states for the sequential two-step priming scheme. SVs reversibly dock at
1325 empty release sites (ES) and become fusion-competent by undergoing a sequence of two
1326 priming steps. After initial docking, SVs in the loosely docked state (LS) reversibly transition to
1327 the tightly docked state (TS) from which they undergo fusion upon AP arrival with the probability
1328 P_r. Vacated sites become immediately available for SV docking and priming. Transitions
1329 represented by dashed lines occur instantaneously, while those represented by solid lines occur
1330 with rate constants as indicated. Forward transition rate constants are Ca^{2+}-dependent. For the
1331 sequential two-step priming scheme, P_r, and total number of sites (N_{total}) were constrained to the
1332 same values for *Rac1*$^{+/+}$ and *Rac1*$^{-/-}$ synapses and only parameters determining the kinetics of
1333 the two priming steps were allowed to differ between genotypes. (**B2**) Dependence of k_1 (top
1334 panel) and k_2 (bottom panel) on cytosolic [Ca^{2+}] for *Rac1*$^{+/+}$ (black) and *Rac1*$^{-/-}$ (orange)
1335 synapses. The inset illustrates the time course of the effective [Ca^{2+}] during a 500 Hz train
1336 consisting of 40 stimuli. (**B3**) Predictions of the sequential two-step model (lines) for the time
1337 course of the fractional recovery of $EPSC_{test}$ after 500 Hz conditioning trains superimposed onto
1338 experimental data for *Rac1*$^{+/+}$ (black circles) and *Rac1*$^{-/-}$ (orange triangles) synapses (data from
1339 Fig. 5A3). (**B4**) Predictions of the sequential two-step model (lines) for the time course of STP
1340 during 50 Hz and 500 Hz trains superimposed onto experimental data (circles) for *Rac1*$^{+/+}$
1341 (black, top panel) and *Rac1*$^{-/-}$ (orange, bottom panel) synapses. (**B5**) Model predictions for the
1342 time course of STP during 50 Hz and 500 Hz trains for *Rac1*$^{+/+}$ (gray and black) and *Rac1*$^{-/-}$
1343 (light and dark orange) synapses shown superimposed to facilitate comparison.
1344
1345 **Fig. 6 – Figure supplement 1: Model predictions and parameters of simple single pool**
1346 **models fitted to *Rac1*$^{+/+}$ and *Rac1*$^{-/-}$ STP and recovery data sets.**

1347 (**A**) Model predictions for synaptic STP during regular stimulus trains consisting of 40 APs and
1348 delivered at frequencies from 0.5 to 500 Hz for *Rac1*$^{+/+}$ (**A1**, black) and *Rac1*$^{-/-}$ (**A2**, orange)
1349 synapses. Note the strongly enhanced initial synaptic strength but similar steady-state release at
1350 the highest stimulus frequency. (**B**) Model predictions for the paired-pulse ratio
1351 (PPR = $EPSC_2/EPSC_1$) for *Rac1*$^{+/+}$ (black circles) and *Rac1*$^{-/-}$ (orange triangles) synapses.
1352 While *Rac1*$^{+/+}$ synapses show substantial net facilitation at ISIs of 2 and 5 ms, net facilitation is
1353 absent from for *Rac1*$^{-/-}$ synapses. (**D**) Model parameters for *Rac1*$^{+/+}$ (**D1**, black) and *Rac1*$^{-/-}$
1354 (**D2**, orange) synapses. Parameter values that differ between the models for *Rac1*$^{+/+}$ and *Rac1*$^{-/-}$
1355 synapses are listed in bold. For details, please refer to Lin et al. (2022). For converting EPSC
1356 amplitudes measured in the presence of 1 mM kynurenic acid into quantal content, a quantal
1357 size of q = 7.48 pA was assumed.
1358
1359 **Fig. 6 – Figure supplement 2: Model predictions and parameters of sequential two-step**
1360 **models fitted to *Rac1*$^{+/+}$ and *Rac1*$^{-/-}$ STP and recovery data sets.**
1361 (**A**) Model predictions for synaptic STP during regular stimulus trains consisting of 40 APs and
1362 delivered at frequencies from 0.5 to 500 Hz for *Rac1*$^{+/+}$ (**A1**, black) and *Rac1*$^{-/-}$ (**A2**, orange)
1363 synapses. Note the strongly enhanced initial synaptic strength but similar steady-state release at
1364 the highest stimulus frequency. (**B**) Model predictions for the paired-pulse ratio
1365 (PPR = $EPSC_2/EPSC_1$) for *Rac1*$^{+/+}$ (black circles) and *Rac1*$^{-/-}$ (orange triangles) synapses.
1366 While *Rac1*$^{+/+}$ synapses show substantial net facilitation at ISIs of 2 and 5 ms, net facilitation is
1367 absent from for *Rac1*$^{-/-}$ synapses. (**D**) Model parameters for *Rac1*$^{+/+}$ (**D1**, black) and *Rac1*$^{-/-}$
1368 (**D2**, orange) synapses. Parameter values that differ between the models for *Rac1*$^{+/+}$ and *Rac1*$^{-/-}$
1369 synapses are listed in bold. For details, please refer to Lin et al. (2022). For converting EPSC
1370 amplitudes measured in the presence of 1 mM kynurenic acid into quantal content, a quantal
1371 size of q = 7.48 pA was assumed.
1372

1373 **Fig. 7: Alterations in presynaptic release probability did not impair the reliability of action**
1374 **potential generation during *in vivo*-like activity.** (**A1**) AP firing was recorded in response to *in*
1375 *vivo*-like stimulation patterns derived from responses to sinusoidal amplitude-modulated sounds
1376 at different modulation frequencies. Raster plot shows three representative stimulation patterns.
1377 (**A2**) Representative traces of loose-patch recordings during afferent fiber stimulation with in
1378 vivo-like activity for *Rac1*$^{+/+}$ (black) and *Rac1*$^{-/-}$ (orange). Triangles indicate the stimulus time
1379 points. Stimulus artifacts were blanked for clarity. (**B1**) Fraction of successful AP generation was
1380 not different between *Rac1*$^{+/+}$ and *Rac1*$^{-/-}$ independent of modulation frequency (**B2**) AP jitter
1381 defined as the standard deviation of AP latencies was not changed in *Rac1*$^{-/-}$ neither for the
1382 complete stimulus nor as a function of amplitude modulation frequency. (**C1**) AP jitter and AP
1383 delay were largely independent of preceding inter-spike interval. (**C2**) AP jitter and AP delay as a
1384 function of preceding activity level. The preceding activity was calculated as the sum of all
1385 preceding APs (green, S_{-1}, S_{-2}, …, S_{-n}) weighted by their temporal distance to the AP under
1386 observation (purple, W_{-1}, W_{-2}, …, W_{-n}). The weighting was implemented as an exponentially
1387 decaying kernel (blue shaded area). Note the increased AP jitter and AP delay in *Rac1*$^{-/-}$ at
1388 higher activity levels. All data shown in the figure and the detailed results of statistical tests are
1389 part of the supplementary file.
1390 **Figure 7 – source data 1:** Excel file containing the data shown in Figure 7 and the results of
1391 statistical analysis.
1392
1393 **Fig. 8: Proposed model of Rac1's presynaptic role in regulating synaptic transmission.** In
1394 the proposed model, loss of Rac1 results in changes in F-actin at the active zone, thereby
1395 reducing the physical barrier between SVs and the plasma membrane resulting in increased
1396 synaptic strength through faster priming and potentially higher P_r.
1397
1398

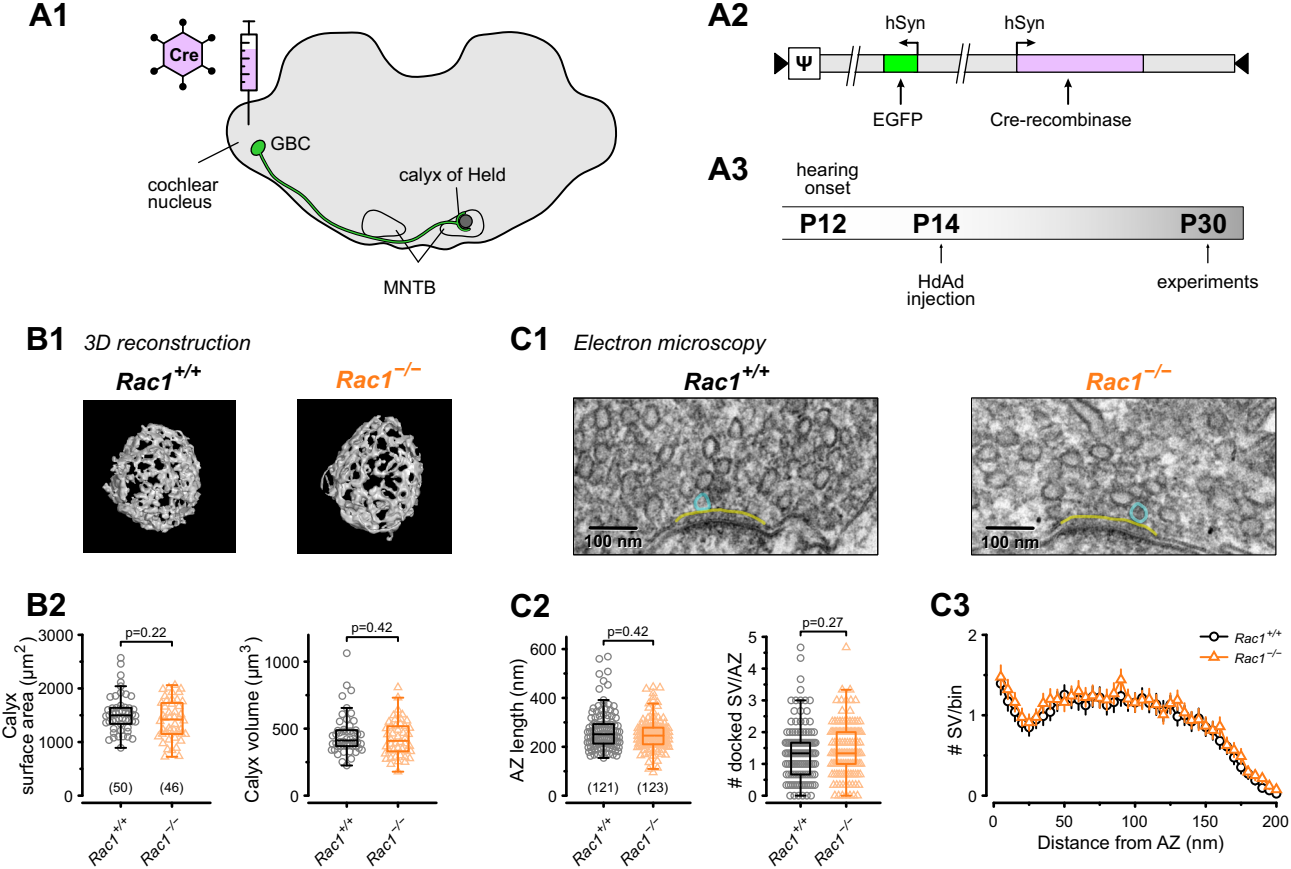
A1
Cre
GBC
cochlear nucleus
calyx of Held
MNTB
A2
hSyn
hSyn
Ψ
EGFP
Cre-recombinase
A3
hearing onset
P12
P14
P30
HdAd injection
experiments
B1
3D reconstruction
Rac1+/+
Rac1−/−
C1
Electron microscopy
Rac1+/+
Rac1−/−
100 nm
100 nm
B2
Calyx surface area (µm2)
p=0.22
(50)
(46)
Calyx volume (µm3)
p=0.42
Rac1+/+
Rac1−/−
C2
AZ length (nm)
p=0.42
(121)
(123)
# docked SV/AZ
p=0.27
Rac1+/+
Rac1−/−
C3
Rac1+/+
Rac1−/−
SV/bin
Distance from AZ (nm)

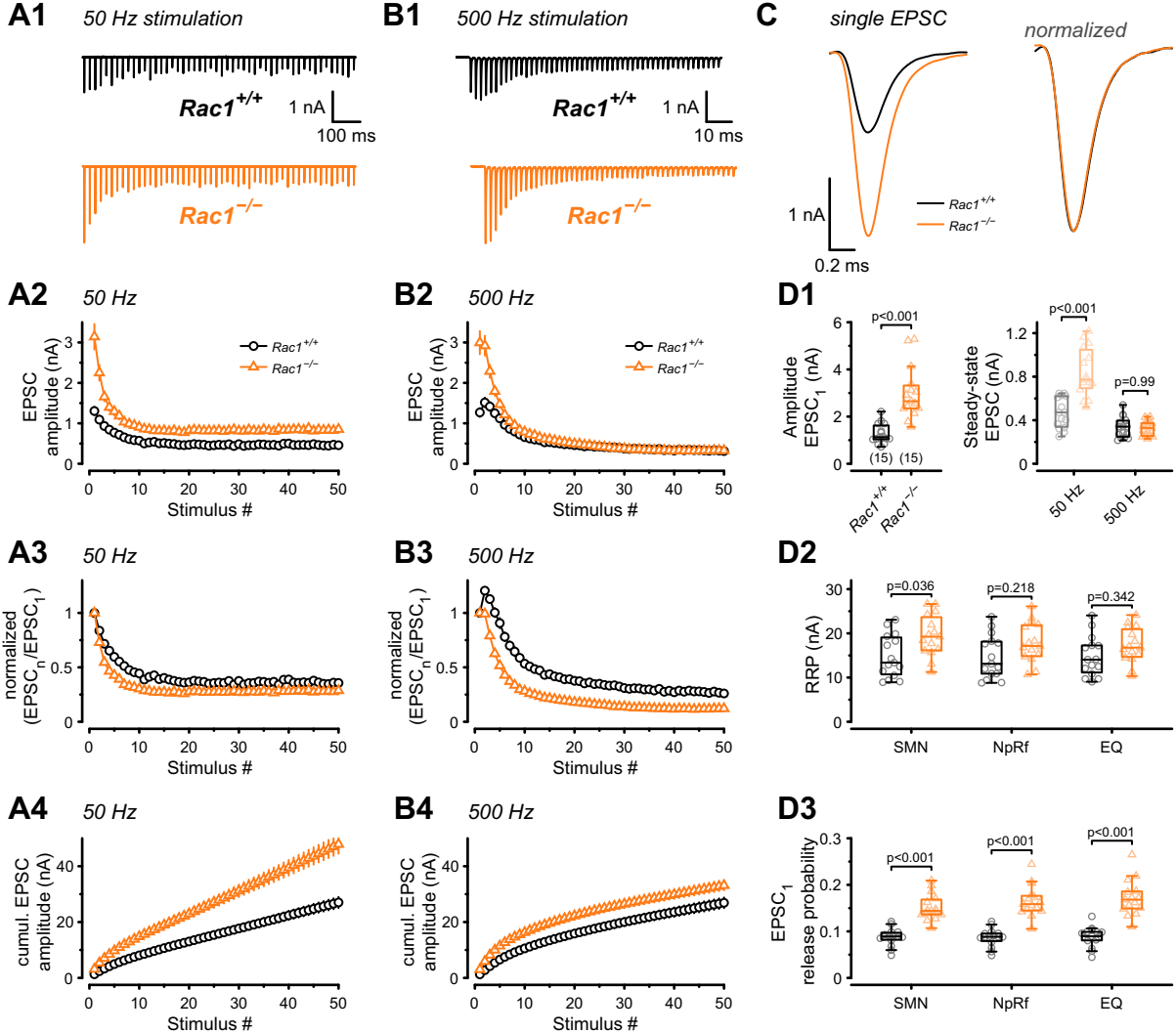
A1
50 Hz stimulation
Rac1+/+
1 nA
100 ms
Rac1−/−
B1
500 Hz stimulation
Rac1+/+
1 nA
10 ms
Rac1−/−
C
single EPSC
normalized
1 nA
0.2 ms
Rac1+/+
Rac1−/−
A2
50 Hz
EPSC amplitude (nA)
Stimulus #
B2
500 Hz
EPSC amplitude (nA)
Stimulus #
D1
Amplitude EPSC1 (nA)
p<0.001
(15) (15)
Rac1+/+
Rac1−/−
Steady-state EPSC (nA)
p<0.001
p=0.99
50 Hz
500 Hz
A3
50 Hz
normalized (EPSCn/EPSC1)
Stimulus #
B3
500 Hz
normalized (EPSCn/EPSC1)
Stimulus #
D2
RRP (nA)
p=0.036
p=0.218
p=0.342
SMN
NpRf
EQ
A4
50 Hz
cumul. EPSC amplitude (nA)
Stimulus #
B4
500 Hz
cumul. EPSC amplitude (nA)
Stimulus #
D3
EPSC1 release probability
p<0.001
p<0.001
p<0.001
SMN
NpRf
EQ

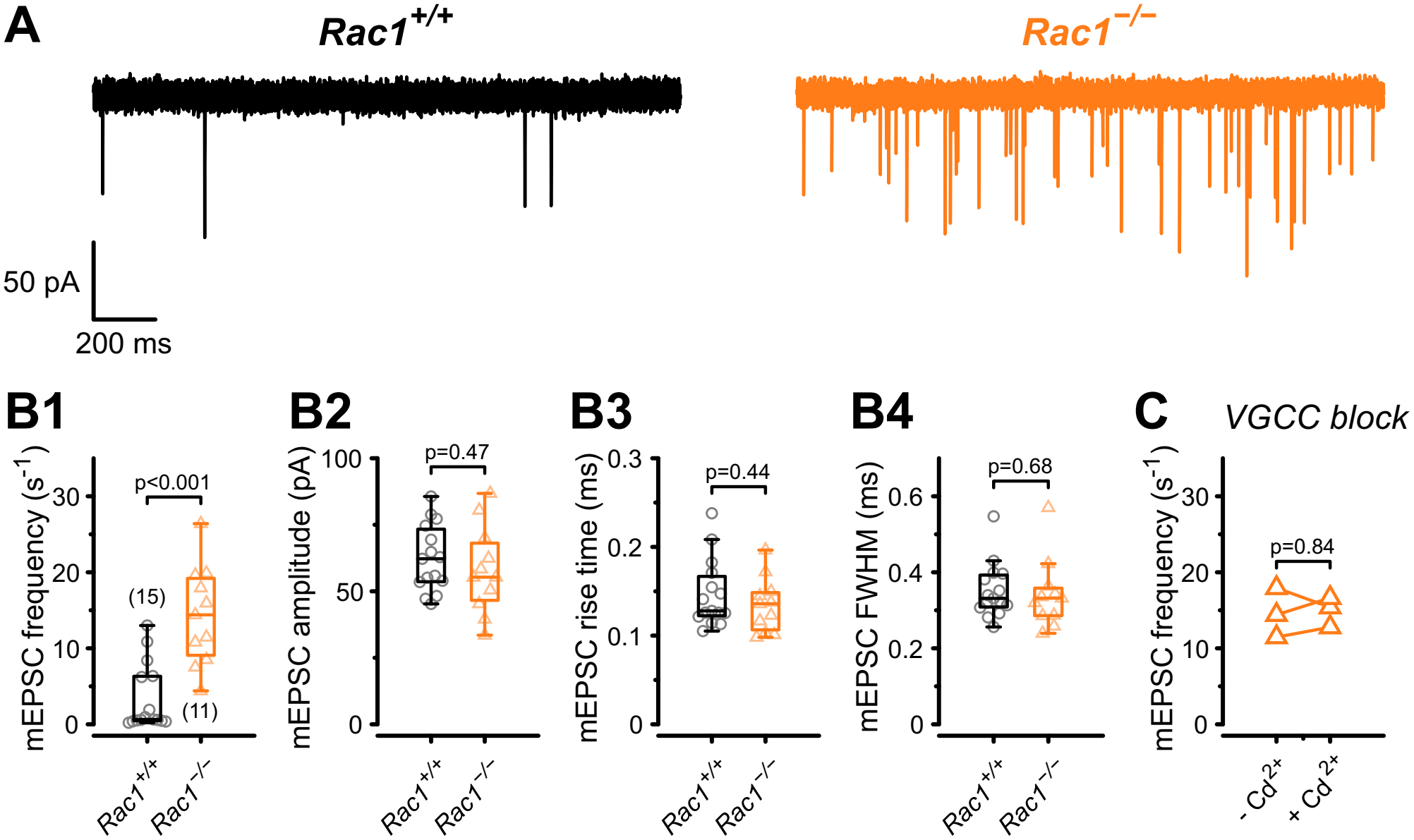
A
Rac1+/+
Rac1−/−
50 pA
200 ms
B1
mEPSC frequency (s-1)
p<0.001
(15)
(11)
B2
mEPSC amplitude (pA)
p=0.47
B3
mEPSC rise time (ms)
p=0.44
B4
mEPSC FWHM (ms)
p=0.68
C
VGCC block
mEPSC frequency (s-1)
p=0.84
- Cd2+
+ Cd2+

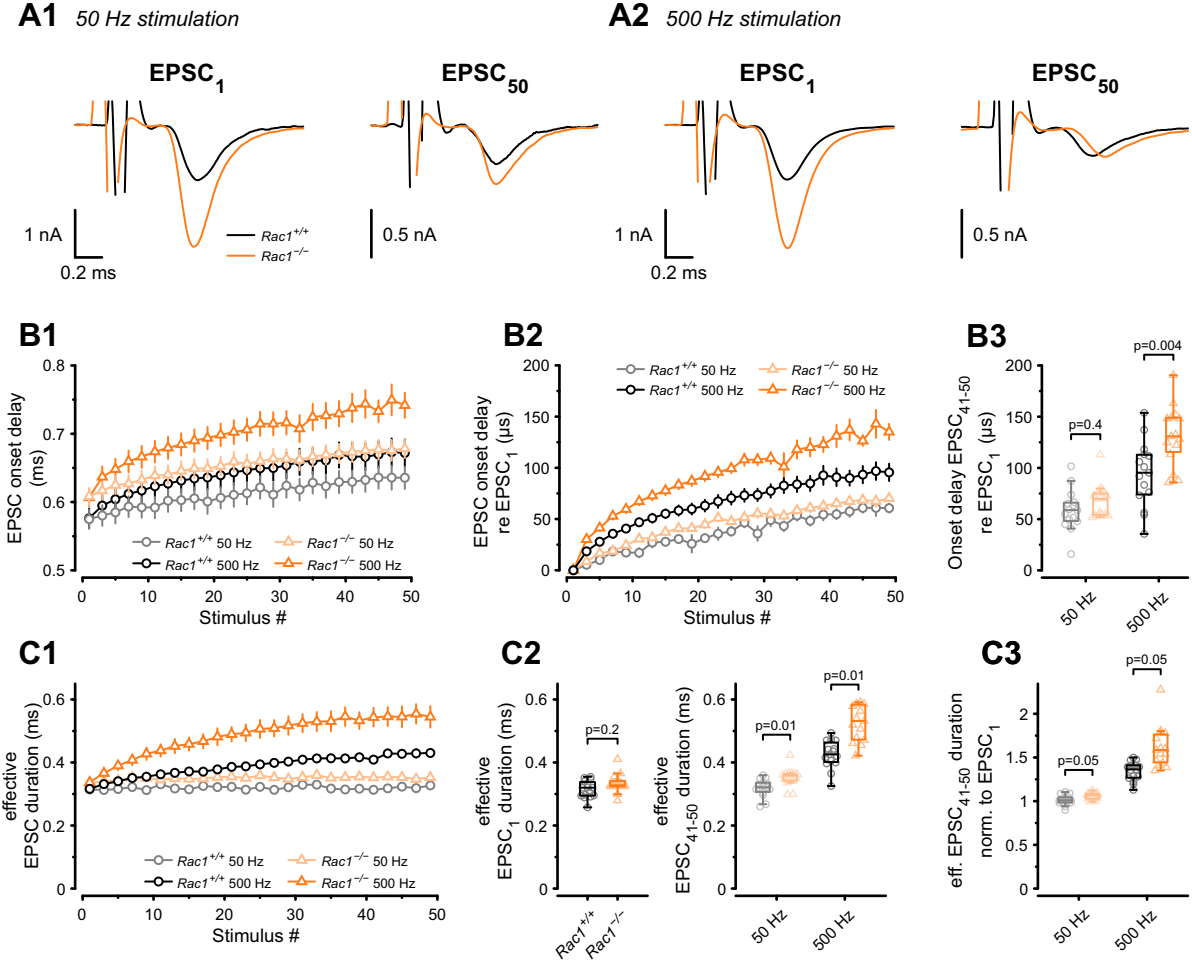
A1 50 Hz stimulation
A2 500 Hz stimulation
EPSC1
EPSC50
EPSC1
EPSC50
1 nA
0.2 ms
Rac1+/+
Rac1−/−
0.5 nA
1 nA
0.2 ms
0.5 nA
B1
EPSC onset delay (ms)
Rac1+/+ 50 Hz
Rac1+/+ 500 Hz
Rac1−/− 50 Hz
Rac1−/− 500 Hz
Stimulus #
B2
EPSC onset delay re EPSC1 (µs)
Stimulus #
B3
Onset delay EPSC41-50 re EPSC1 (µs)
p=0.4
p=0.004
50 Hz
500 Hz
C1
effective EPSC duration (ms)
Stimulus #
C2
effective EPSC1 duration (ms)
p=0.2
Rac1+/+
Rac1−/−
effective EPSC41-50 duration (ms)
p=0.01
p=0.01
50 Hz
500 Hz
C3
eff. EPSC41-50 duration norm. to EPSC1
p=0.05
p=0.05
50 Hz
500 Hz

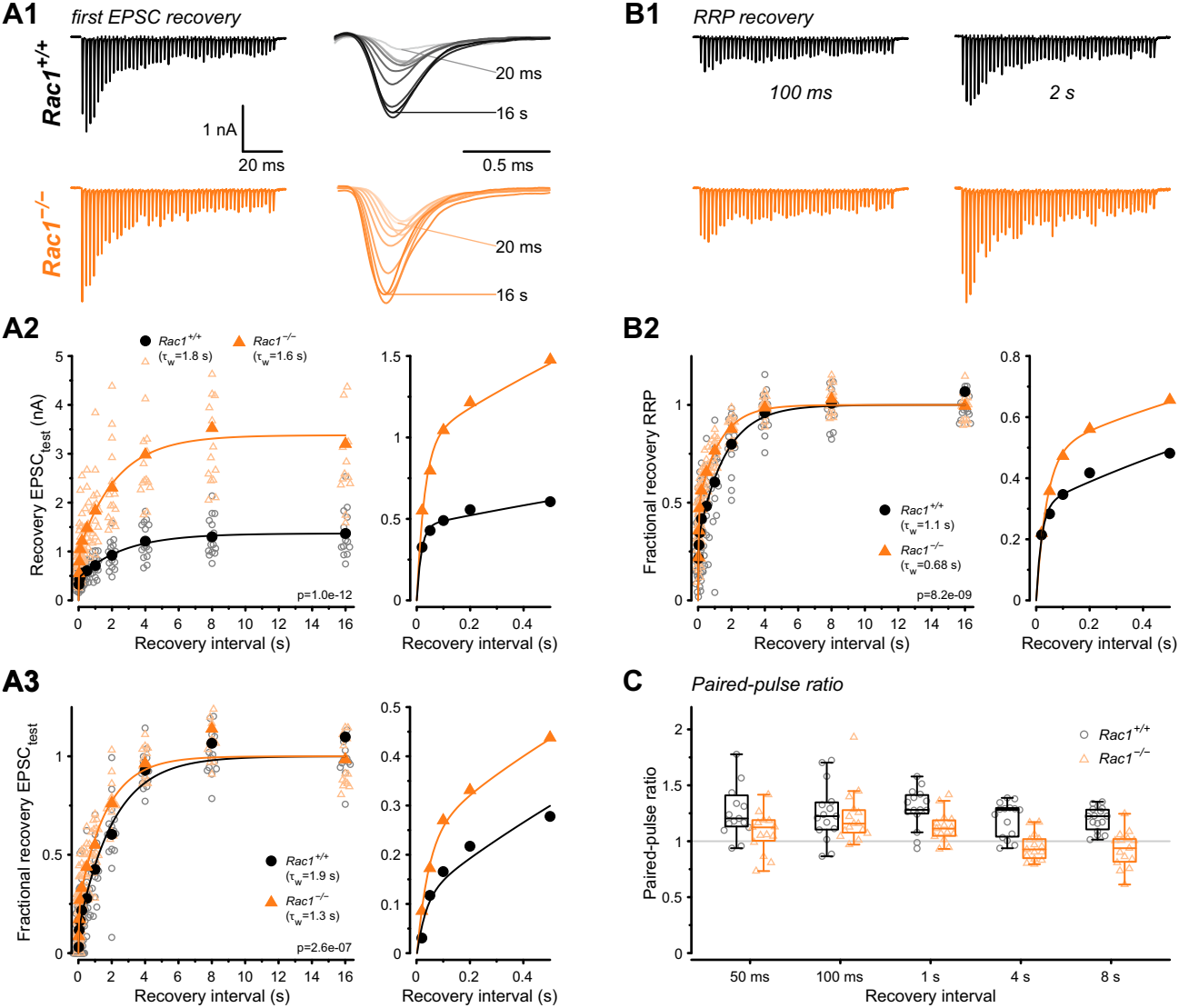
A1
first EPSC recovery
Rac1+/+
1 nA
20 ms
20 ms
16 s
0.5 ms
Rac1−/−
20 ms
16 s
B1
RRP recovery
100 ms
2 s
A2
Rac1+/+ (τw=1.8 s)
Rac1−/− (τw=1.6 s)
Recovery EPSCtest (nA)
p=1.0e-12
Recovery interval (s)
Recovery interval (s)
B2
Fractional recovery RRP
Rac1+/+ (τw=1.1 s)
Rac1−/− (τw=0.68 s)
p=8.2e-09
Recovery interval (s)
Recovery interval (s)
A3
Fractional recovery EPSCtest
Rac1+/+ (τw=1.9 s)
Rac1−/− (τw=1.3 s)
p=2.6e-07
Recovery interval (s)
Recovery interval (s)
C
Paired-pulse ratio
Rac1+/+
Rac1−/−
Paired-pulse ratio
50 ms
100 ms
1 s
4 s
8 s
Recovery interval

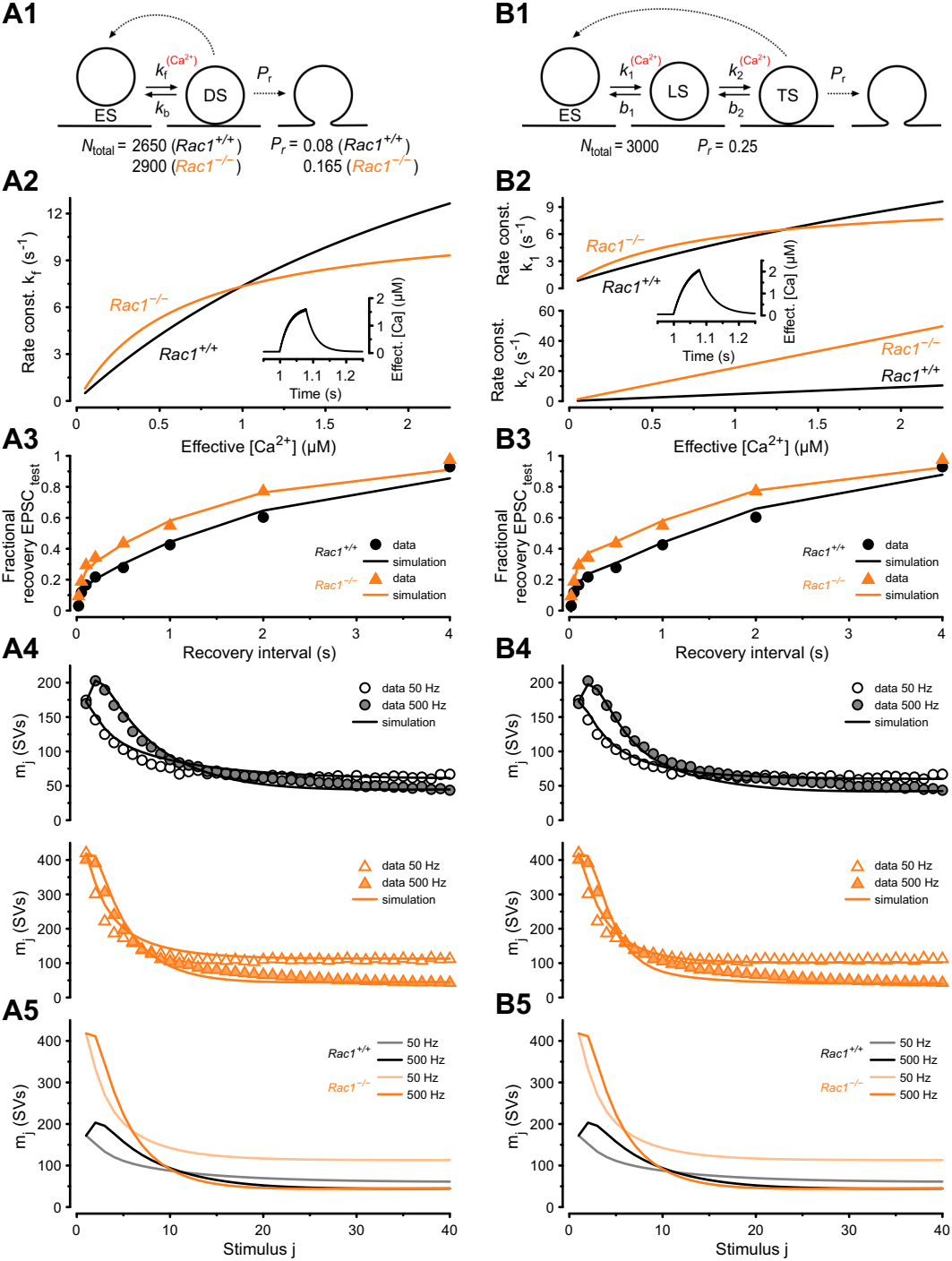
A1
ES
DS
$k_f^{(Ca^{2+})}$
k_b
P_r
N_{total} = 2650 ($Rac1^{+/+}$)
2900 ($Rac1^{-/-}$)
P_r = 0.08 ($Rac1^{+/+}$)
0.165 ($Rac1^{-/-}$)
B1
ES
LS
TS
$k_1^{(Ca^{2+})}$
b_1
$k_2^{(Ca^{2+})}$
b_2
P_r
N_{total} = 3000
P_r = 0.25
A2
Rate const. k_f (s^{-1})
$Rac1^{-/-}$
$Rac1^{+/+}$
Effect. [Ca] (μM)
Time (s)
Effective [Ca^{2+}] (μM)
B2
Rate const. k_1 (s^{-1})
Rate const. k_2 (s^{-1})
$Rac1^{-/-}$
$Rac1^{+/+}$
Effect. [Ca] (μM)
Time (s)
Effective [Ca^{2+}] (μM)
A3
Fractional recovery $EPSC_{test}$
$Rac1^{+/+}$ data simulation
$Rac1^{-/-}$ data simulation
Recovery interval (s)
B3
Fractional recovery $EPSC_{test}$
$Rac1^{+/+}$ data simulation
$Rac1^{-/-}$ data simulation
Recovery interval (s)
A4
m_j (SVs)
data 50 Hz
data 500 Hz
simulation
B4
m_j (SVs)
data 50 Hz
data 500 Hz
simulation
A5
m_j (SVs)
$Rac1^{+/+}$ 50 Hz 500 Hz
$Rac1^{-/-}$ 50 Hz 500 Hz
Stimulus j
B5
m_j (SVs)
$Rac1^{+/+}$ 50 Hz 500 Hz
$Rac1^{-/-}$ 50 Hz 500 Hz
Stimulus j

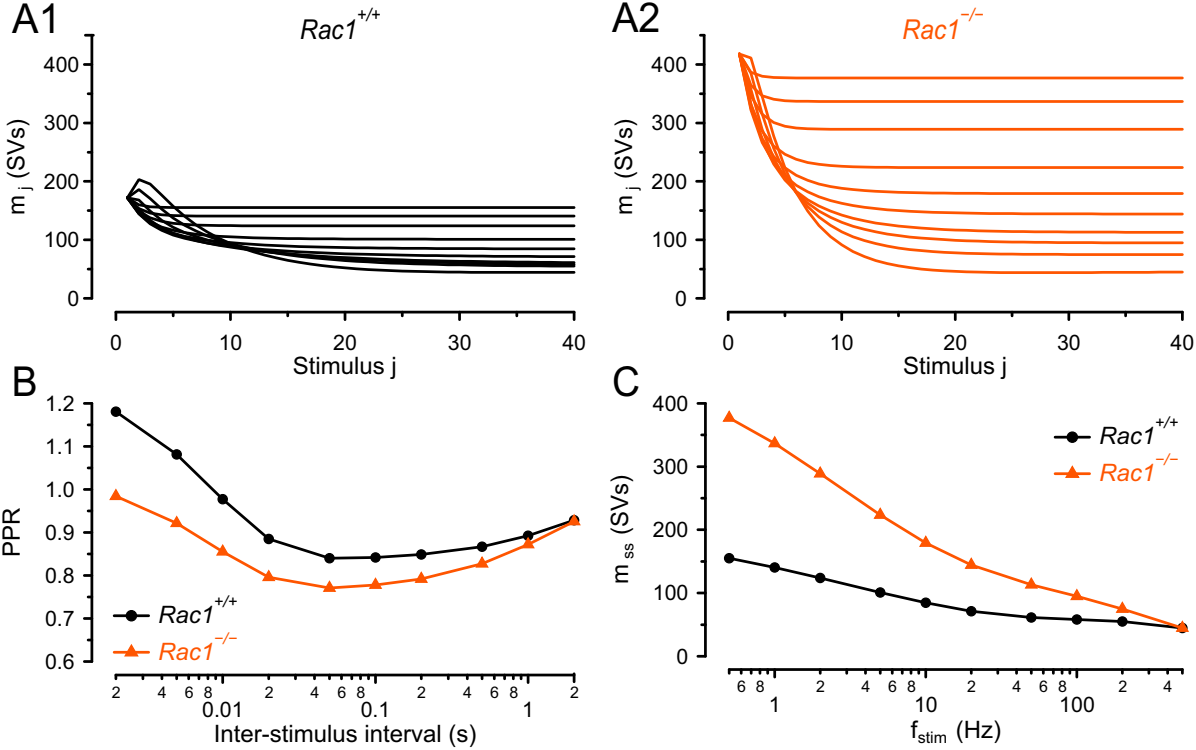

D1

Parameter	Value	Unit
$[Ca^{2+}]$ decay τ	0.028	s
$[Ca^{2+}]$ amplitude	1.0E-07	M
P_r	0.08	
N_{total}	2650	
k_f	0.5	s^{-1}
k_b	0.116	s^{-1}
σ	9.6E+06	s^{-1} M^{-1}
$K_{0.5}$	3.1E-06	M
y_{inc}	0.5	
z_{dec}	0.4	
y_{max}	1.2	
z_{min}	0.75	
τ_y	0.01	s
τ_z	3	s

D2

Parameter	Value	Unit
$[Ca^{2+}]$ decay τ	0.028	s
$[Ca^{2+}]$ amplitude	1.0E-07	M
P_r	**0.165**	
N_{total}	**2900**	
k_f	**0.8**	**s^{-1}**
k_b	0.116	s^{-1}
σ	**1.8E+07**	**s^{-1} M^{-1}**
$K_{0.5}$	**6.6E-07**	**M**
y_{inc}	0.5	
z_{dec}	0.4	
y_{max}	**1.15**	
z_{min}	0.75	
τ_y	0.01	s
τ_z	3	s

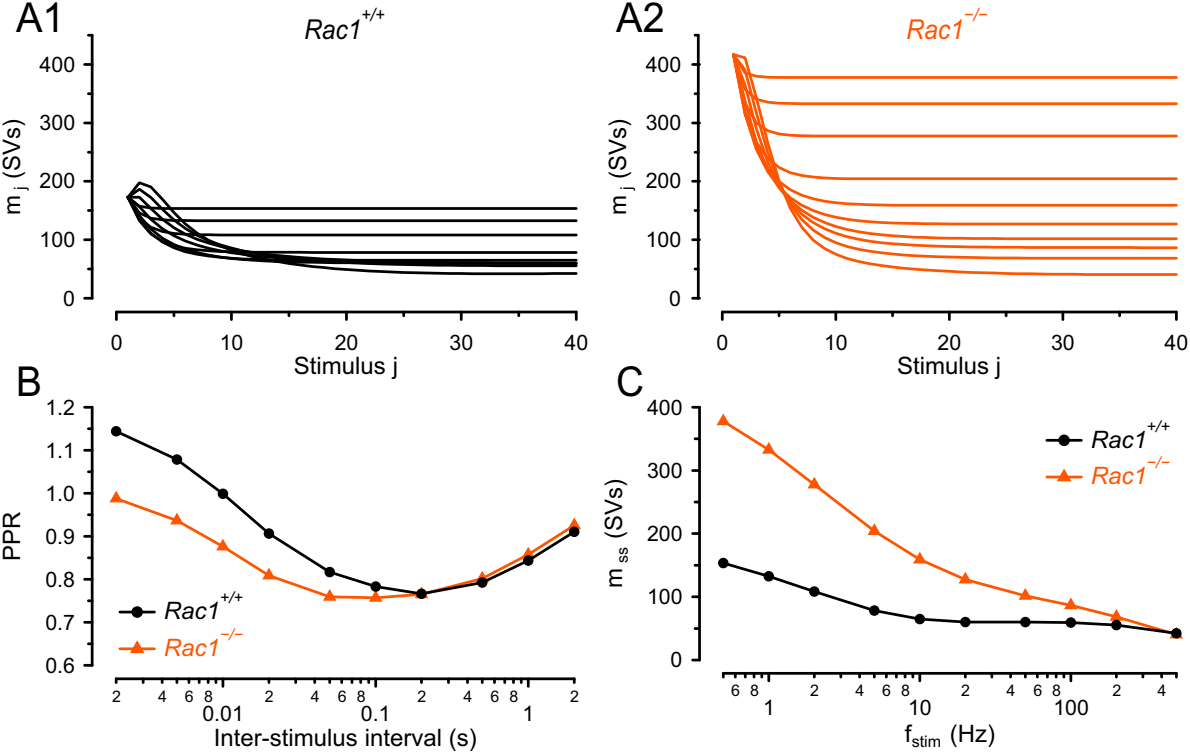

D1

Parameter	Value	Unit
$[Ca^{2+}]$ decay τ	0.043	s
$[Ca^{2+}]$ amplitude	9.5E-08	M
P_r	0.25	
N_{total}	3000	
k_1	0.84	s^{-1}
b_1	0.42	s^{-1}
σ_1	5.7E+06	s^{-1} M^{-1}
k_2	0.31	s^{-1}
b_2	0.69	s^{-1}
σ_2	4.6E+06	s^{-1} M^{-1}
TSL decay τ	0.08	
TSL fraction	0.08	
$K_{0.5}$	5.6E-06	M
y_{inc}	0.34	
z_{dec}	0.4	
y_{max}	1.23	
z_{min}	0.8	
τ_y	0.014	
τ_z	3	

D2

Parameter	Value	Unit
$[Ca^{2+}]$ decay τ	0.043	s
$[Ca^{2+}]$ amplitude	9.5E-08	M
P_r	0.25	
N_{total}	3000	
k_1	**1.05**	**s^{-1}**
b_1	**0.35**	**s^{-1}**
σ_1	**1.2E+07**	**s^{-1} M^{-1}**
k_2	**1.3**	**s^{-1}**
b_2	**0.78**	**s^{-1}**
σ_2	**2.2E+07**	**s^{-1} M^{-1}**
TSL decay τ	0.08	
TSL fraction	0.08	
$K_{0.5}$	**8.5E-07**	**M**
y_{inc}	0.34	
z_{dec}	0.4	
y_{max}	1.23	
z_{min}	0.8	
τ_y	0.014	
τ_z	3	

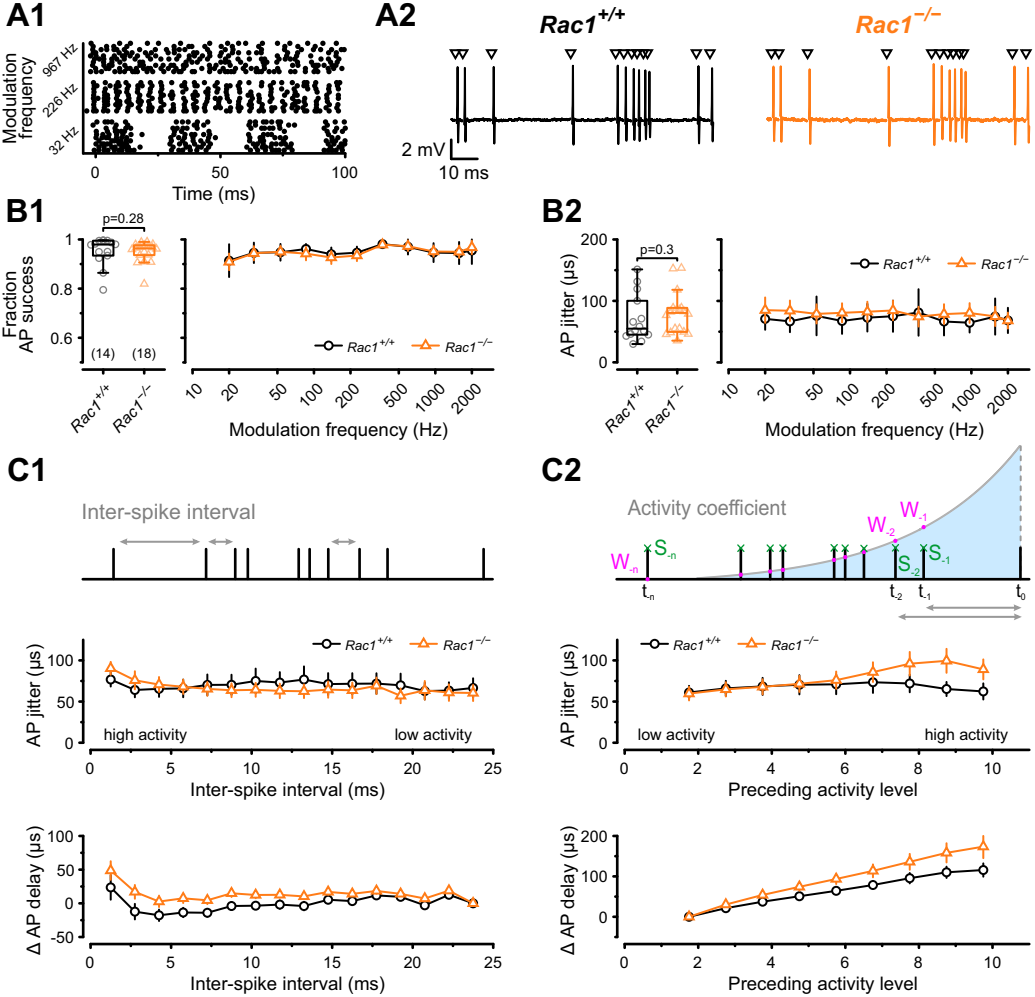
A1
Modulation frequency
967 Hz
226 Hz
32 Hz
0
50
100
Time (ms)
A2
Rac1+/+
Rac1−/−
2 mV
10 ms
B1
p=0.28
Fraction AP success
1
0.8
0.6
(14)
(18)
Rac1+/+
Rac1−/−
10
20
50
100
200
500
1000
2000
Modulation frequency (Hz)
B2
p=0.3
AP jitter (µs)
200
100
0
Rac1+/+
Rac1−/−
10
20
50
100
200
500
1000
2000
Modulation frequency (Hz)
C1
Inter-spike interval
AP jitter (µs)
100
50
0
Rac1+/+
Rac1−/−
high activity
low activity
0
5
10
15
20
25
Inter-spike interval (ms)
Δ AP delay (µs)
100
50
0
-50
0
5
10
15
20
25
Inter-spike interval (ms)
C2
Activity coefficient
W-n
S-n
W-2
W-1
S-2
S-1
tn
t-2
t-1
t0
AP jitter (µs)
100
50
0
Rac1+/+
Rac1−/−
low activity
high activity
0
2
4
6
8
10
Preceding activity level
Δ AP delay (µs)
200
100
0
0
2
4
6
8
10
Preceding activity level

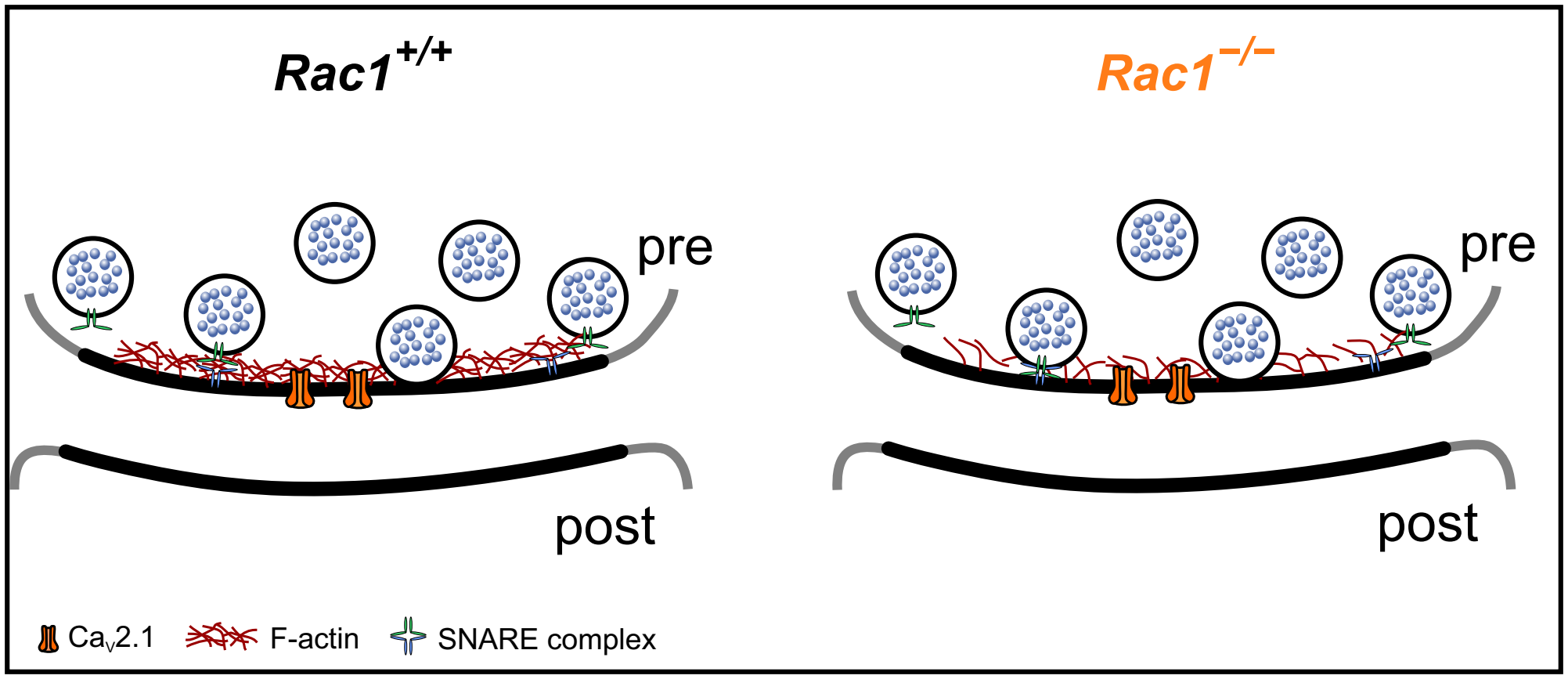
Rac1+/+
Rac1−/−
pre
pre
post
post
CaV2.1
F-actin
SNARE complex